INELASTIC K^+p REACTIONS

AT INCIDENT MOMENTA FROM 1.37 GeV/c TO 2.17 GeV/c

Thesis by

Stewart Christian Loken

In Partial Fulfillment of the Requirements

For the Degree of

Doctor of Philosophy

California Institute of Technology

Pasadena, California

1972

ACKNOWLEDGMENTS

This experiment was performed by a large collaboration: R. Juhala and E. Malamud of NAL; D. Davies, P. Schlein, and W. Slater of UCLA; and B. Barish, R. Gomez, J. Pine and me from Caltech. All the members of the group participated in some part of the experiment, and helped in its successful completion.

Many others contributed to the experiment as well. C. Rosenfeld of Caltech built the gas Cerenkov counter; Art Ogawa, H. Grau and B. Freidler of Caltech built the triads, and helped greatly in the installation of all instrumentation. B. Lockman, R. Poster, and J. Brown of UCLA, T. Boark and J. Cooper of NAL, and B. Garnjost of LRL spent many long hours taking pictures. The hospitality and assistance of G. Eckman and the crew of the LRL 25 inch chamber is also greatly appreciated. The film was measured and the data analysed at UCLA. The assistance of R. Lippman and the scanners at UCLA was invaluable in completing this project.

I wish to thank Drs. Ricardo Gomez and Jerry Pine for their advice and assistance throughout the experiment, and particularly Dr. Barry Barish, my advisor, for his guidance, help and encouragement

during my graduate work at Caltech.

For financial support I am grateful to Caltech.

ABSTRACT

A number of recent experiments have suggested the possibility of a highly inelastic resonance in K^+p scattering. To study the inelastic K^+p reactions, a 400 K exposure has been taken at the L.R.L. 25 inch bubble chamber. The data are spread over seven K^+ momenta between 1.37 and 2.17 GeV/c.

Cross-sections have been measured for the reaction $K\bar{p} \rightarrow pK^o\pi^+$ which is dominated by the quasi-two body channels $K\Delta$ and K^*N. Both these channels are strongly peripheral, as at other momenta. The decay of the Δ is in good agreement with the predictions of the rho-photon analogy of Stodolsky and Sakurai. The data on the K^*p channel show evidence of both pseudo scalar and vector exchange.

Cross-sections for the final state $pK^+\pi^+\pi^-$ shows a strong contribution from the quasi-two body channel $K^*\Delta$. This reaction is also very peripheral even at threshold. The decay angular distributions indicate the reaction is dominated as at higher momenta by a pion exchange mechanism. The data are also in good agreement with the quark model predictions of Bialas and Zalewski for the K^* and Δ decay.

to geanie

TABLE OF CONTENTS

APPENDIX

EXTRACTION OF PARAMETERS FOR QUASI-TWO BODY STATES

FIGURES

xi

TABLES

I. INTRODUCTION

The spectrum of baryon resonances established
by experiment can be explained very successfully as
states of three constituent particles, called quarks,
each of which has strangeness 0 or -1[1]. In this
model, then, it is impossible to form baryon states
with strangeness +1. Such a resonance (usually called
a Z*) would have to consist of at least four quarks
and one antiquark.

A number of recent experiments have suggested a
possible Z* resonance in K^+p scattering. The total
K^+p cross-section[2] and elastic cross-section[3]
are shown in figure 1. The elastic cross-section
falls smoothly with momentum but the total cross-
section data show a peak at 1.35 GeV/c and a second
shoulder at about 1.9 GeV/c. A fit to the first
bump suggests a resonance of 4 mb at a mass of 1910
MeV. The full width at half height is 180 MeV and
the value of $(J + \frac{1}{2})X$ is .3 where J is the spin and
X the elasticity. The second bump corresponds to a
.2 mb peak at 2190 MeV with a width of 120 MeV and
$(J + \frac{1}{2})X = .03$.

Analysis of the elastic differential cross-
section and proton polarization data also suggests
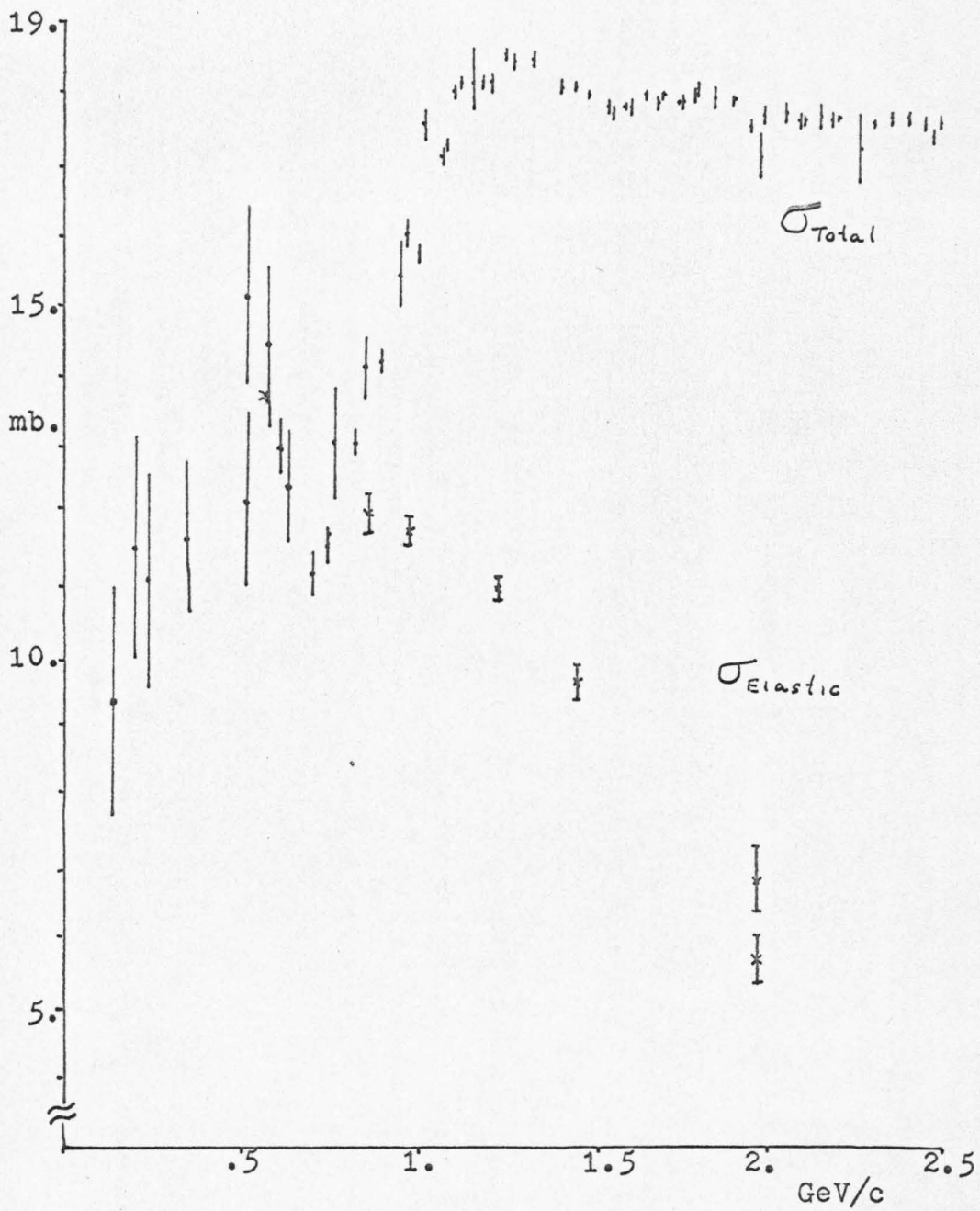
Figure 1. K⁺p Elastic and Total Cross-sections

a possible resonance[4]. Some of the solutions, from both energy dependent and energy independent analyses, indicate a possible resonance in the $P_{3/2}$ partial wave at an incident momentum between 1.3 and 1.9 GeV/c. Figure 2 shows a typical solution for the P wave amplitudes. These analyses show that the resonance, if it exists, is very inelastic (elasticities vary between .1 and .45). They also suggest that the speed, the rate of change of phase shift with energy, is not consistent with resonance behavior.

All experiments which show some resonance features share the common characteristic of a small elasticity. For this reason, it is of interest to study the inelastic channels in K^+p system. In an earlier experiment, Bland et al.[5], studied single pion production at incident momenta between .84 GeV/c and 1.37 GeV/c. They conclude that the first bump in the total cross-section is a threshold effect, resulting from the opening of the inelastic channel $K\Delta$. There is no indication of a Z* resonance over the momentum range of their experiment.

It is the purpose of this experiment to extend the study of the inelastic K^+p reactions. The lowest
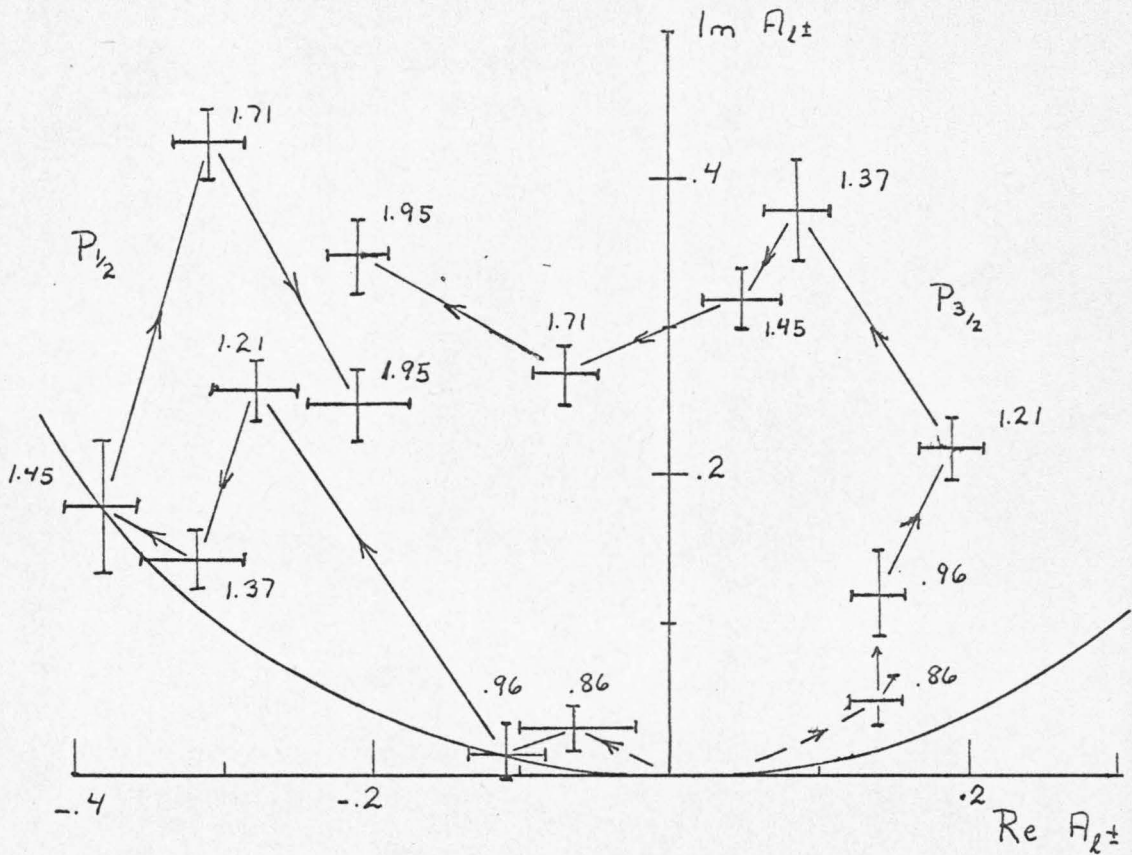
Figure 2.   Representative Phase Shift Solution.
The P$_{3/2}$ Phase Shift has been fitted to a resonance
amplitude.   The parameters of the resonance are:
Mass, 1950 ± 100 MeV (momentum, 1.34 GeV/c);   Total
Width, 180 MeV;   Elasticity, .28;   Kato et al. (4)

momentum 1.37 overlaps the data of Bland. The
maximum momentum of the beam transport system was
2.2 GeV/c.

In this experiment we will consider single
pion and two pion production. Quasi-two body
processes contribute significantly to the pion
production reactions and much of the analysis will
be devoted to these states.

The details of the experiment will be described
in parts II - IV. In parts V and VI, cross-
sections are discussed for single and two pion
states, and for the quasi-two body channels
respectively. The production and decay of reson-
ances in the quasi-two body reactions is studied
in part VII. The angular distributions are com-
pared with data at higher and lower momenta to
look for evidence of possible direct channel
effects.

II. DESCRIPTION OF THE EXPERIMENT

A. Beam

The experiment consisted of 400 K pictures taken in the Lawrence Radiation Laboratory 25 inch hydrogen bubble chamber. These were distributed over seven K^+ momenta, spaced between 1.37 GeV/c and 2.17 GeV/c.

The K^+ beam was produced at a platinum target in the Bevatron external proton beam, and was transported to the bubble chamber in the Bevatron beam K9 (see figure 3)[6]. The beam momentum was restricted to about ±1% by slits at the first horizontal focus. Two stages of mass separation, each consisting of an electrostatic separator, and slits at the vertical focus, were used to remove most of the pions.

A Freon 12 gas threshold Cerenkov counter was installed in the quadrupole magnet directly in front of the bubble chamber. This counted pions at all momenta except 1.37 and 1.52 GeV/c, and gave us a continuous monitor of beam contamination. The pions amounted to about 5% at 2.17 GeV/c but were less than 2% at all momenta below 1.94 GeV/c. A marker light was flashed in the chamber for each frame where one of the particles was a pion.
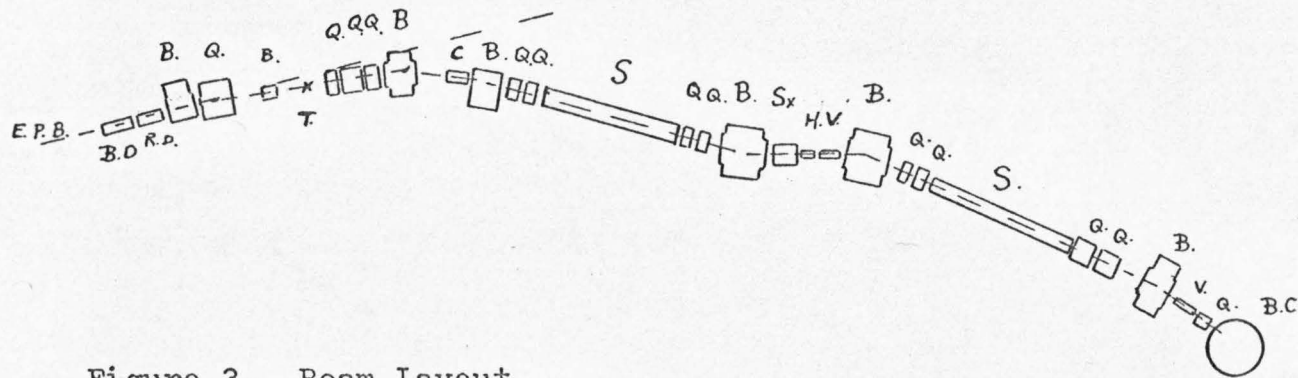
Figure 3. Beam Layout
The elements of the beam are denoted by: E.P.B., Bevatron
External Proton Beam; B.D., Beam Destroyer; R.D., Rapid
Deflector Magnet; T., Production Target; B., Bending
Magnet; Q., Quadrupole Magnet; Sx., Sextupole Magnet;
S., Electrostatic Separator; V., Vertically Aperturing
Slits; H., Horizontally Aperturing Slits; B.C., Bubble
Chamber.

A triad of scintillation counters set on the
pion image at each mass slit allowed us to continuously
check beam steering and focussing to maintain a
constant flux at the bubble chamber. For each pulse,
we took a picture only if there were more than five,
and less than fifteen tracks in the chamber.

To further control the number of tracks in
each picture, a beam destroyer magnet was installed
upstream of the production target. This was pulsed
rapidly when eleven tracks had been counted at the
scintillation counter in front of the bubble chamber.
The proton beam was deflected from the production
target into the beam dump.

B. Scanning and Measuring

The film was simultaneously scanned and measured
on SMP's (Scanning and Measuring Projectors) at UCLA.
The SMP facility consists of five projectors connected
to an IBM 360/44 computer. The computer filtered
the track measurements, checked for continuity of
vertex and track data points, and output track points
in each of three views at about 3 cm. intervals.

C. System of Analysis Programs

The output of the SMP system was processed
through the TVGP-SQUAW-ARROW system developed at
LRL to produce a data summary tape containing the
physical quantities describing each event which are
needed in the subsequent physics analysis.

TVGP (three view geometry program[7]) inputs on
SMP tape and performs a space reconstruction of each
track. A curve is fitted through the measured track
points by a least-squares method, and the angles and
curvature are determined for each track. In order to
properly account for the energy loss by ionization,
the fit for each track is tried for each possible
particle. The output of TVGP consists of azimuth,
dip, and inverse projected momentum at the beginning
and end of each track, for each possible mass, as well
as the errors for these errors. Film setting errors
and Coulomb scattering errors are included.

The kinematic fitting program SQUAW[8] inputs a
TVGP output tape, and fits the measured momenta to
kinematic hypotheses. The fit was done by minimizing
the χ^2 function subject to the analytic constraints
appropriate to the hypothesis being tested. The four
energy-momentum conservation equations provide four

constraints minus the number of unmeasured variables involved in a given hypothesis. These constraints are introduced by the method of Lagrange Multipliers, and an iteration procedure is used to minimize χ^2. SQUAW outputs the fitted quantities and errors for each hypothesis which achieves a confidence level greater than 10^{-5}.

ARROW[9] inputs a SQUAW output tape and selects those events of interest for a particular analysis. The output data summary tape consists of identification information for the event, and the four vectors for the reaction fit.

III. SCANNING, MEASURING AND FITTING

A. <u>Results of First Scan</u>

All the film taken in the experiment was carefully
scanned for interactions of interest (see figure 4).
Topologies we have studied include all events with
more than two outgoing visible tracks, and all those
with a visible decay of a neutral particle. If all
reaction particles are detected in the chamber, these
correspond to the reactions

$$K^+ \to \pi^+\pi^+\pi^- \qquad\qquad \text{3 prong}$$
$$K^+p \to pK^o\pi^+ \qquad\qquad \text{2 prong V}$$
$$K^+p \to pK^+\pi^+\pi^- \qquad\qquad \text{4 prong}$$
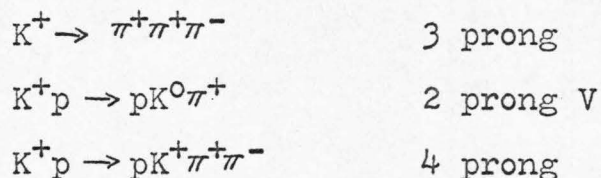
We have, in addition, required that the incoming
track have approximately the same curvature, and that
the production vertex fall within a volume which
corresponded to about 80% of the chamber length.
The reason for this fiducial volume cut was to ensure
a constant detection efficiency, and to provide as
long a decay length as possible for the neutral K's.

Table 1 lists the number of frames scanned at
each momentum, and the number of events of each
topology found and measured on the first pass. All
these events have been processed through the system

Figure 4. Measured Topologies
a. Three prong, b. Two prong V, c. Four prong

TABLE 1

MEASUREMENT SUMMARY

momentum	frames	3 prongs	2 prong V	4 prong
2.17	53319	638	1270	1792
2.07	51157	695	1195	1340
1.94	54679	678	1270	1165
1.81	53643	734	1234	906
1.67	50936	660	1058	432
1.52	48257	802	1069	160
1.37	54298	677	807	71

of programs described in the previous section, and
the results of this fitting will be discussed in a
later section. We will first consider the efficiency
of this scanning in finding events of each desired
topology.

B. Scanning Efficiency

Because we wish to measure production cross-
sections, and the dependence of these cross-sections
on incident momentum, it is important to determine
the efficiency of the scanners at finding events.
To do this we have re-scanned about half the film
at each momentum. We have then compared these two
scans frame by frame.

If we assume that the scanning losses are random,
we can easily measure the efficiency of each scan.

$$\text{first pass} \quad N_1 = \epsilon_1 N_0$$
$$\text{second pass} \quad N_2 = \epsilon_2 N_0$$
$$\text{both passes} \quad N_{12} = \epsilon_1 \epsilon_2 N_0$$
$$\text{efficiency of pass 1} = \epsilon_1 = N_{12} / N_2$$

This efficiency is used to correct the number
of events of each topology found in the first scan.
The average correction for this inefficiency was

5% and showed no systematic dependence on momentum
or topology.

C. Fitting Failures

Approximately 10% of all measured events cannot
be successfully reconstructed in the TVGP program.
These are events for which the scatter of the measured
points from the fitted curve is outside the predicted
errors from Coulomb scattering and the measuring
machine errors. Some of these events have been
studied on the scanning table and appear to be
associated with crossing tracks or low contrast
film.

About half of the failing events have been re-
measured and the passage rate is again approximately
the same as the first pass. The failure rate is
constant over all momenta and is the same for all
reactions so that there is no correction to the
cross-sections for this inefficiency.

Some of the measured events did not pass any
reaction fit in SQUAW. These had too large a χ^2
in the final fit, or took too many steps to find a
χ^2 minimum. When these events were re-measured, the
passage rate was consistent with the first measurement
rate.

The ratio of events fitting the possible reactions in the second measurement was in good agreement with the first measurement results. To correct the cross-sections for this fitting inefficiency we assume that the events that were not re-measured, and those that failed the second fitting were distributed in the same ratio. The correction varied slightly with momentum and averaged 21% for events with a neutral decay V and 14% for the four prong events. All three prong events found on film fitted the tau decay hypothesis and no correction was made for fitting.

D. Separation of Reaction Fits

Because of the measurement errors in the momenta and angles, many events can pass more than one reaction fit. The program ARROW, discussed briefly in section II, is used to sort out the reaction fits and to determine the most probable hypothesis.

For the events which have no missing neutral, that is the four constraint fits, ambiguities between possible fits are not a serious problem. Fewer than 5% of these had more than one fit. For events with one missing neutral the reduced kinematic constraints allow more ambiguities. Here about 35% of the

measurements fit more than one reaction hypothesis.

From many previous bubble chamber experiments, two guidelines have been established to separate hypotheses. If an event corresponds to a reaction where there is an undetected particle in the chamber, it cannot pass a reaction fit with four kinematic constraints. For hypotheses with the same number of constraints, the X^2 of the fit is a reliable criteria for choosing the correct reaction.

From these guidelines we have created a badness function B defined by

$$B = X^2 + 5 * \text{(number of kinematic constraints)}$$

This corresponds qualitatively to the confidence level but is more heavily weighted in favor of the four constraint reactions. We will always assume that the correct fit is the one given by minimum badness.

In order to evaluate the effectiveness of the event selection, we have scanned a sample of events and have compared the predicted ionization for each track with the darkness of the track in the chamber In all cases where the reactions could be distinguished by ionization, the fit favored by this was the fit

favored by the badness criterion.   It was never

possible to rule out the preferred fit by ionization.

IV. CROSS-SECTION DETERMINATION

A. Normalization

The number of events in each reaction final state has been determined from the kinematic fitting. To determine the cross-sections for the reactions of interest, we must also know the number of incident K^+ 's and the number of protons.

The primary normalization for this experiment is the decay of the K^+ in the tau mode, $\pi^+\pi^+\pi^-$.

Using the tau decays, the cross-section is given by the formula

$$\sigma = \frac{N(\text{interactions})}{N(\text{decays})} * \frac{B}{\eta c \tau} * \frac{A_H}{\rho_H N_A}$$

where

A_H(atomic weight of hydrogen) = 1.008

N_A(Arogadro's number) = $6.0225 * 10^{23}$ mole^{-1}

ρ_H(density of hydrogen in chamber) = .0608 g cm^{-3}

$\eta = \beta\gamma = P_{\text{beam}} / M_{K^+}$

$c = 2.998 * 10^{10}$ cm sec^{-1}

$\tau(K^+$ lifetime) = $1.235 * 10^{-8}$ sec

$B(K^+$ branching ration into the τ mode) = .056

Since the tau decays were measured at the same time as the reactions and with the same fiducial

volume criteria, this normalization should be free of any systematic bias. To check this we have also used a beam track count, and a total cross-section scan.

B. Beam Track Count

We have scanned every fifth roll of film, and have recorded the number of tracks in every tenth frame. In this scan, care was taken to ensure that the tracks counted were only those that could have had measureable events. No off-beam or off-momentum tracks were included.

Using the data from this scan, we have determined the average number of tracks per frame at each momentum. This does vary slightly with momentum because of variations in beam tuning and in Bevatron operating conditions.

The total beam track length has been determined at each momentum using the total number of frames, the fiducial volume length and the track average.

C. Total Cross-section

When the second scan was made to measure the scanning efficiency the two-prong events were also recorded. For this sample, then, we have all events of all topologies, and hence have measured a total

cross-section. By comparing this to the accurate total cross-sections measured by counter experiments[2], we have determined the beam track length at each momentum.

D. Comparison of Normalizations

The beam track lengths determined by the three different methods are given in table 2 along with the uncertainty in each determination from counting statistics. The results are in good agreement, and appear to show only random fluctuations. We have decided, however, not to combine the results of the three methods.

The beam track count has two disadvantages which make it less reliable. It is difficult to be sure that the tracks counted really correspond to the tracks for the measured sample. In addition, the method requires an accurate knowledge of the length of the chamber used. The fiducial length was defined by marks on the chamber lens, and when the beam moved vertically, the effective length changed.

In principle the total cross-section should be a reliable normalization since the length cancels out as it does with the tau decays. The total cross-section scan, however, is much more sensitive

TABLE 2

BEAM TRACK LENGTH

momentum GeV/c	tau decay x 10^6 cm	σ_{total} x 10^6 cm	track count x 10^6 cm
2.17	24.2 ± .9	23.6 ± .3	21.9 ± 1.1
2.07	21.6 ± .8	21.5 ± .3	20.2 ± 1.0
1.94	20.0 ± .8	20.6 ± .3	20.1 ± 1.0
1.81	23.6 ± .9	26.0 ± .3	20.4 ± 1.0
1.67	19.8 ± .8	18.5 ± .3	18.8 ± .9
1.52	19.5 ± .8	21.8 ± .4	17.1 ± .9
1.37	13.9 ± .6	13.2 ± .4	14.9 ± .8

to scanning biases than the tau's. It is very difficult
for scanners to detect the very small angle deflections
of forward scattered particles, and the momentum
transfer to the proton is too small for it to be seen
in the chamber. On the other hand, all the K^+ decays
having only one charged particle in the final state
look very much like scattering events. We have not
measured this scanning efficiency, and have not fitted
the two prongs in TVGP and SQUAW, so that it is
impossible to know the effect of these difficulties.

The tau decays were measured at the same time
as the reaction sample, and the scanning efficiency
has been determined in the second pass. They have
all been fitted in the TVGP-SQUAW programs so that
all fitting inefficiencies tend to cancel. We have,
therefore, used only the tau decays in determining
the cross-sections presented in this paper.

E. $\underline{K^0 \text{ Escape Correction}}$

For those reactions corresponding to the two-
prong V topology we must make a correction for the
unseen K^0 events. This includes the factor for the
number of K^0's that are in the K^0_L state, and a factor
for the $K^0_S \rightarrow \pi^+\pi^-$ branching ratio.

We must also include a correction for the K^o_s's
which escape from the chamber. This factor has been
calculated by averaging over the K^o momentum, and
angles, and averaging over the fiducial length for
the production vertex. The correction varied from
6% at 2.17 GeV/c to 2% at the lowest momentum. The
dependence on momentum and angle is small and can
be ignored in the calculation of differential cross-
sections and angular distributions.

F. Pion Contamination

Even after the two stages of mass separation,
there still remained a few pions in the K beam. The
pion contamination at each momentum is given in
table 3. In order to determine the effect of this
in our event sample, we took one roll of film at each
momentum with the beam tuned on π's. These frames
were scanned, measured and fitted in the same way as
the K^+ data. Table 3 shows the results of this scanning
and fitting. For all momenta, we have an effective
pion contamination of at most 1%. This will be
neglected in all the subsequent analysis.

TABLE 3
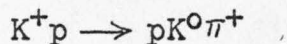
PION CONTAMINATION

momentum GeV/c	Cerenkov counts	4 C fit passage	π events/frame / K events/frame	effective pion contamination
2.17	4.3%	10%	2.3	1%
2.07	3.2%	10%	2.4	.8%
1.94	1.2%	8%	2.7	.3%
1.81	1.0%	5%	2.8	.2%
1.67	.8%	1%	2.6	.0
1.52	---	0	3.1	.0
1.37	---	0	2.9	.0

V. SINGLE PION AND TWO PION PRODUCTION

A. $pK^o\pi^+$ Final State

In this experiment we have studied only one single pion reaction

$$K^+p \longrightarrow pK^o\pi^+$$

The cross-sections for this final state are presented in table 4 and in figure 5. The data from previous experiments[5, 10] are also shown in the figure. The cross-section rises sharply with beam momentum from about .8 GeV/c, and reaches a peak at about 1.3 GeV/c, very close to the bump noted earlier in the total cross-section. Above 1.4 GeV/c there is a very smooth fall off with momentum.

B. $NK\pi$ Cross-section

To better understand the behavior of the single pion production channels, we have included in figure 5 the cross-sections for the two reactions not measured in this experiment.

$$K^+p \longrightarrow pK^+\pi^o$$
$$\longrightarrow nK^+\pi^+$$
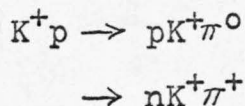
At any momentum where all final states are

TABLE 4

SINGLE PION PRODUCTION CROSS-SECTIONS

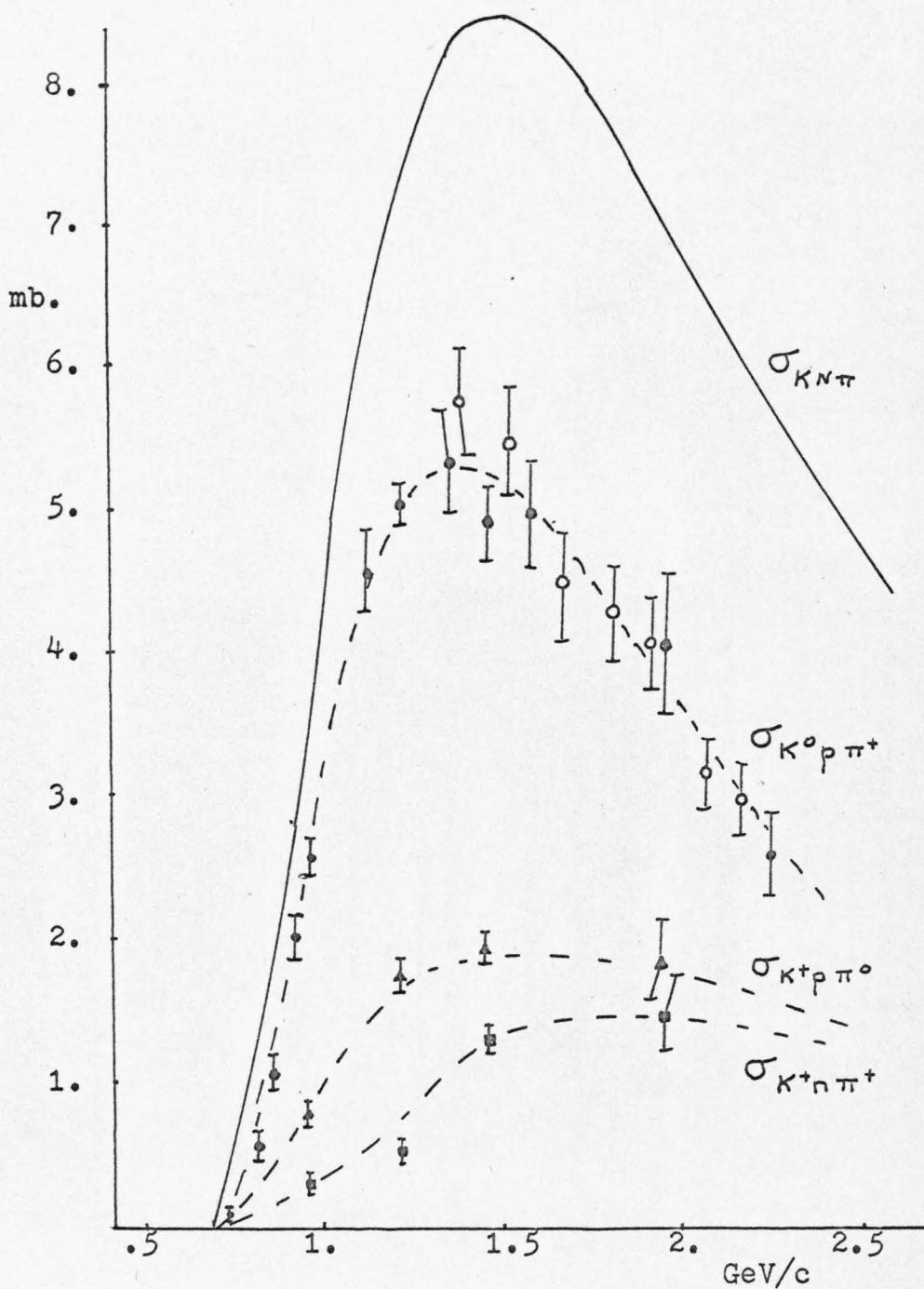| momentum GeV/c	$\sigma(K^+p \rightarrow K^0p\pi^+)$ mb.
2.17	$3.06 \pm .31$
2.07	$3.21 \pm .25$
1.94	$4.09 \pm .35$
1.81	$4.29 \pm .33$
1.67	$4.54 \pm .40$
1.52	$5.52 \pm .37$
1.37	$5.85 \pm .61$

Figure 5. Single Pion Production Cross-sections
The open symbols refer to this experiment, the solid
to reference 10 .

measured, we can easily obtain the $KN\pi$ cross-sections.
We have used an interpolation technique where data were
not available and the results are also shown in figure 5
As in the case of the $pK^0\pi^+$ we see a sharp rise and
then a more gradual fall off with increasing momentum.

The threshold for single pion production is a
momentum of .520 GeV/c. The cross-section, however,
is very small until about .8 GeV/c, the threshold for
production of the quasi-two body channel $K\Delta$. We
will return to this point in our discussion of all
quasi-two body channels in the next section.

C. Two Pion Production

In this experiment we have measured three reactions
having two pions in the final state.

$$K^+p \rightarrow pK^+\pi^+\pi^-$$
$$\rightarrow pK^0\pi^+\pi^0$$
$$\rightarrow nK^0\pi^+\pi^+$$
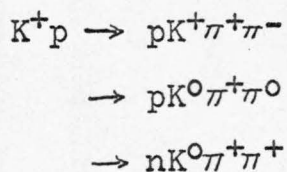
There are two other final states.

$$K^+p \rightarrow pK^+\pi^0\pi^0$$
$$\rightarrow nK^+\pi^+\pi^0$$
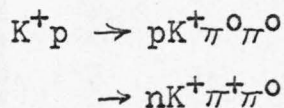
These have two neutrals in the final state and

cannot be separated in the reaction fitting programs.

The cross-sections measured in this experiment are given in table 5 and are presented in figure 6. The figure also includes data from a number of other experiments[11].

The threshold for two pion production is .82 GeV/c, whereas the threshold for the quasi-two body channel K*Δ is 1.74 GeV/c. The data suggest that this channel contributes very strongly to the two pion reactions.

If we assume that these reactions are dominated by this simple state, we can estimate, using Clebsch-Gordan coefficients, the contribution from the two unmeasured reactions. This has been done in figure 6 to calculate the KNππ cross-section.

TABLE 5

TWO PION PRODUCTION CROSS-SECTION

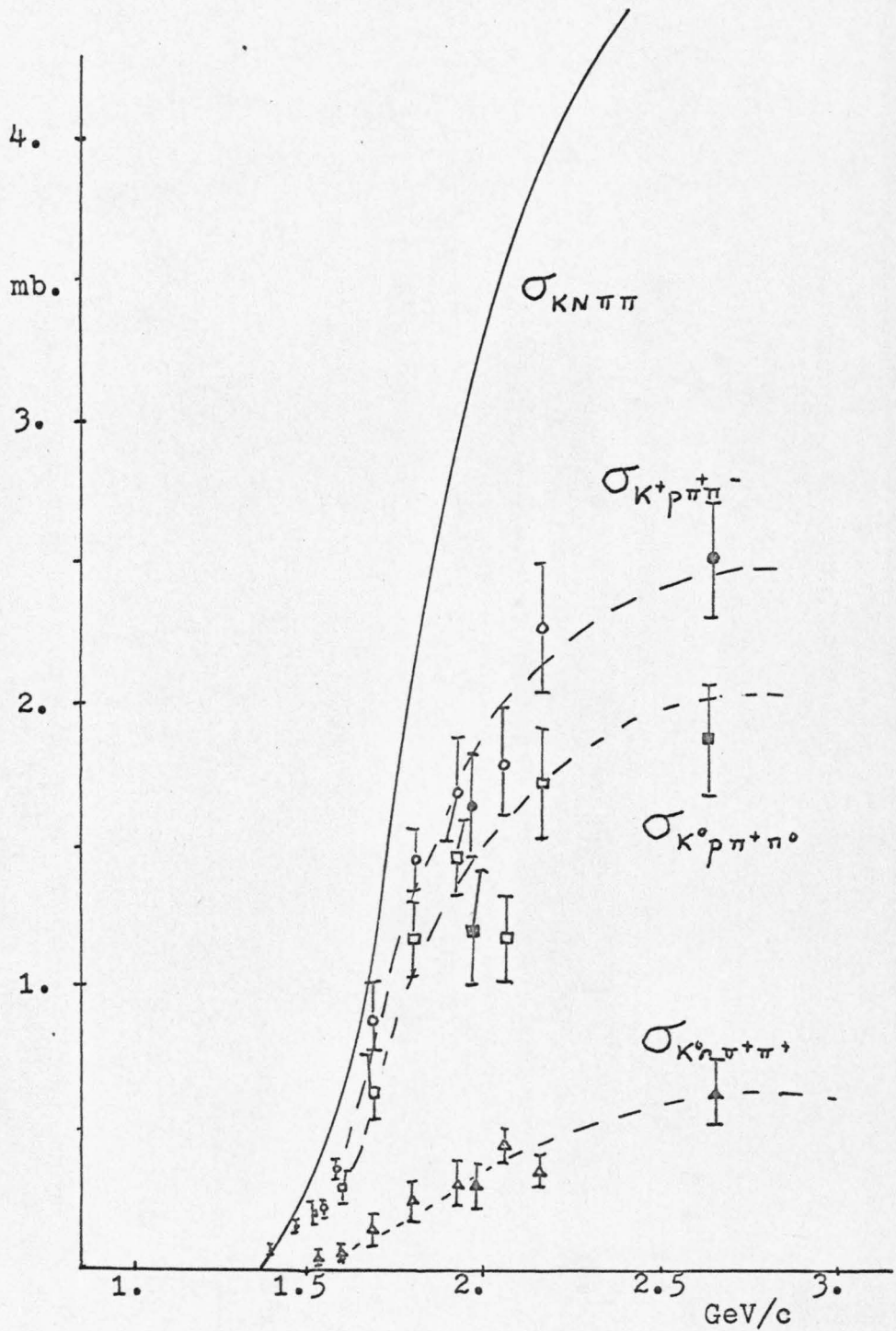| momentum	$\sigma(K^+ p \to K^+ p \pi^+ \pi^-)$	$\sigma(K^+ p \to K^0 p \pi^+ \pi^0)$	$\sigma(K^+ p \to K^0 n \pi^+ \pi^+)$
2.17	$2.28 \pm .16$	$1.75 \pm .2$	$.38 \pm .06$
2.07	$1.82 \pm .11$	$1.19 \pm .15$	$.43 \pm .06$
1.94	$1.72 \pm .12$	$1.50 \pm .17$	$.34 \pm .04$
1.81	$1.47 \pm .09$	$1.20 \pm .15$	$.26 \pm .04$
1.67	$.88 \pm .07$	$.64 \pm .09$	$.17 \pm .04$
1.52	$.24 \pm .08$	$.26 \pm .05$	$.04 \pm .02$
1.37	$.09 \pm .03$	$.12 \pm .03$	$.04 \pm .02$

Figure 6. Two Pion Production Cross-sections
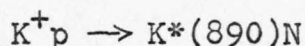Open symbols refer to this experiment, solid
to reference 11 .

VI. QUASI-TWO BODY REACTIONS

A. Single Pion Production

We have already guessed, from very simple threshold
considerations, that the reaction

$$K^+p \longrightarrow K\Delta(1236)$$
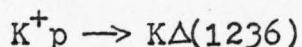
is an important part of the single pion production.
There is, in addition, the reaction

$$K^+p \longrightarrow K*(890)N$$

which would also be expected to contribute.

In table 6 we present the predictions of charge
independence for the various charge states in the
$KN\pi$ final state. The final state $pK^o\pi^+$ is richest
in both $K\Delta$ and $K*N$ production. This is the cleanest
sample from the point of view of fitting ambiguities
and is the only reaction we will consider in this
analysis.

Our interest in the states $K\Delta$ and $K*N$ makes the
choice of variables for a Dalitz plot obvious.
Figure 7 shows plots of $p\pi^+$ effective mass squared
versus $K^o\pi^+$ effective mass squared. The presence of
both resonant channels is evident at all momenta.

TABLE 6

RATIO OF CHARGE STATES IN K^+p REACTIONS

single pion production

charge state	quasi-two body channel	
	$K\Delta$	$K*N$
$pK^0\pi^+$	9	2
$pK^+\pi^0$	2	1
$nK^+\pi^+$	1	0

two pion production

charge state	quasi-two body channel
	$K*\Delta$
$pK^+\pi^+\pi^-$	18
$pK^0\pi^+\pi^0$	13
$nK^0\pi^+\pi^+$	2
$nK^+\pi^+\pi^0$	1
$pK^+\pi^0\pi^0$	2
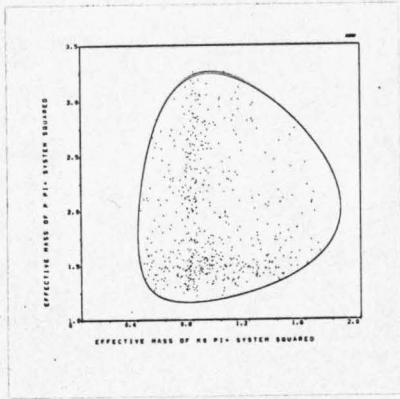
a.
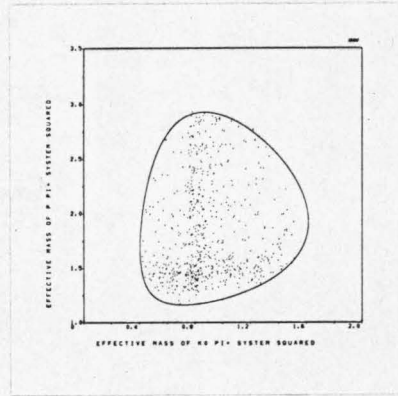
b.
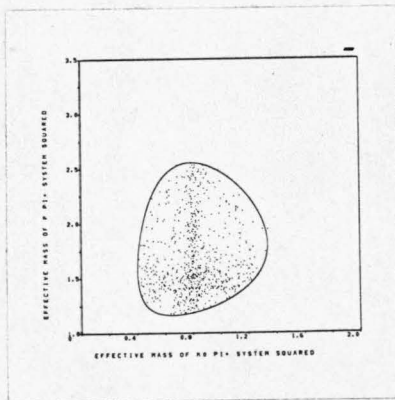
c.

d.

Figure 7. Dalitz plots for the Reaction $K^+p \rightarrow pK^°\pi^+$ at four momenta: a.) 2.17 GeV/c b.) 1.94 GeV/c c.) 1.67 GeV/c d.) 1.37 GeV/c

B. <u>KΔ and K*N Cross-sections</u>

The properties of Dalitz plots and the extraction
of parameters for the quasi-two body channels are
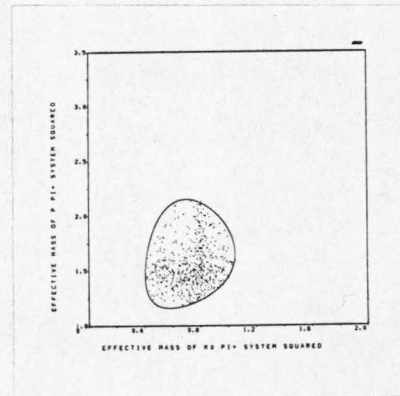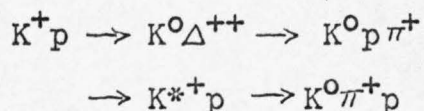reviewed in appendix I. Using these techniques, the
cross-sections for the reactions

$$K^+p \rightarrow K^o \Delta^{++} \rightarrow K^o p \pi^+$$
$$\rightarrow K^{*+}p \rightarrow K^o \pi^+ p$$

have been calculated and are given in table 7 and
table 8.

Using the Clebsch-Gordan coefficients of table 6
we have also calculated the total KΔ and K*N cross-
sections, which are shown in figure 8. Data from
other experiments[10] are also presented in the figure.

The behavior of the KNπ cross-section is clearly
dominated by these two reactions, not only in the
threshold region but at higher momenta as well. At
2.5 GeV/c it appears that the two channels account for
about 80% of the single pion production.

C. <u>K*Δ Interference</u>

In the region of the Dalitz plot where the K*
and Δ bands cross, it is impossible to determine
whether the reaction proceeded through the KΔ or

TABLE 7

CROSS-SECTIONS FOR KΔ PRODUCTION

momentum GeV/c	$\sigma(K^+p \to K^o\Delta^{++})$ mb.	$\sigma(K^+p \to K\Delta)$ mb.
2.17	1.13 ± .17	1.51 ± .23
2.07	1.27 ± .19	1.70 ± .25
1.94	1.53 ± .23	2.04 ± .30
1.81	1.86 ± .27	2.48 ± .36
1.67	1.92 ± .35	2.56 ± .47
1.52	2.22 ± .39	2.96 ± .52
1.37	3.14 ± .46	4.18 ± .61

TABLE 8

CROSS-SECTIONS FOR K*N PRODUCTION

momentum	$\sigma(K^+p \to K^{*+}p)$	$\sigma(K^+p \to K^*N)$
2.17	.92 ± .14	1.38 ± .21
2.07	1.11 ± .18	1.66 ± .27
1.94	1.30 ± .20	1.94 ± .30
1.81	1.46 ± .21	2.19 ± .31
1.67	1.52 ± .25	2.28 ± .37
1.52	1.88 ± .29	2.82 ± .43
1.37	2.02 ± .32	3.02 ± .47
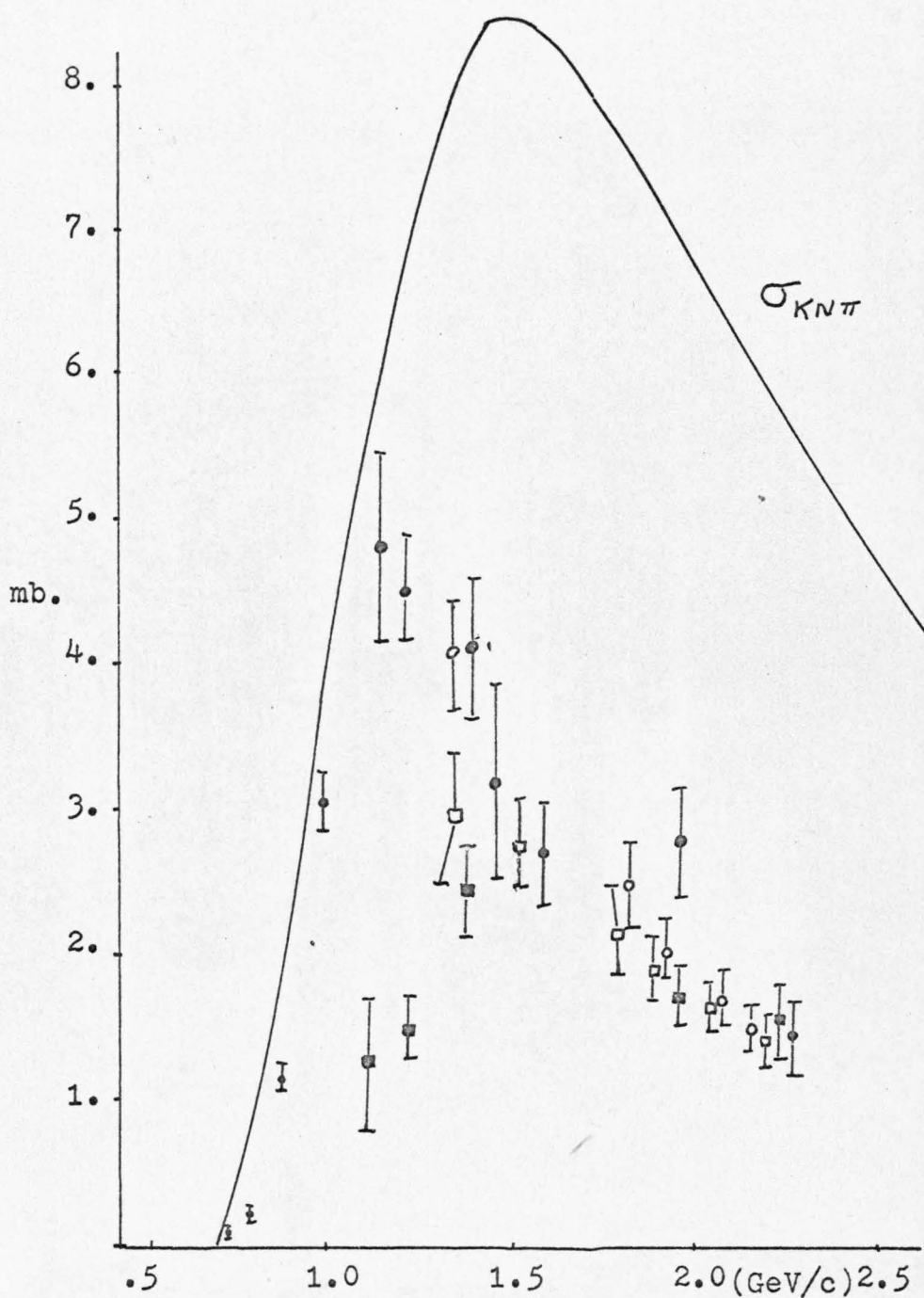
Figure 8.   Cross-sections for K△ and K*N
Production.   Data for K△ shown by ⚐ and ⚑ ; K*N by ⚏
and ⚐.   The open symbols refer to this experiment,
solid to reference 10.

K*N intermediate state. In this case the Dalitz plot density is not just the sum of the squares of the production amplitude, but can include an interference term.

In appendix I we have discribed a technique for measuring the contribution of such an interference term. The results of the analysis are shown in table 9. There appears to be no net enhancement in the interference region and we will neglect interference in the discussion of the $K\Delta$ and K*N final states.

D. Two Pion Production

The only quasi-two body reaction with a threshold in the range of this experiment is the reaction

$$K^+p \rightarrow K^*(890)\Delta(1236)$$
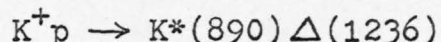
The ratios for the possible charge states have been calculated using isotopic spin Clebsch-Gordan coefficients. The reaction which is richest in resonance production is

$$K^+p \rightarrow pK^+\pi^+\pi^-$$
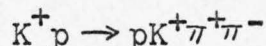
This is the four constraint fit for our four prong sample and is for this reason the cleanest reaction to study. This reaction will be used for all our

TABLE 9

K*-Δ INTERFERENCE CONTRIBUTION
TO THE pK⁰π⁺ FINAL STATE

momentum GeV/c	cross-section mb.
2.17	+.15 ± .07
2.07	-.04 ± .08
1.94	+.31 ± .11
1.81	+.12 ± .08
1.37	+.16 ± .17

studies of the K*Δ state, but first we should return
to the assumption made in determining the $KN\pi\pi$ cross-
section.

The table of coefficients shows that the ratio
of the three measured reactions

$$K^+p \to pK^+\pi^+\pi^-$$
$$pK^0\pi^+\pi^0$$
$$nK^0\pi^+\pi^+$$
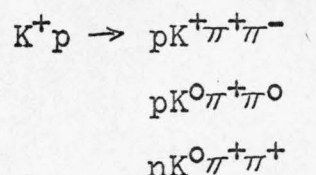
is 18 : 13 : 2. This is in good agreement with the
observed cross-sections, and strengthens our confidence
that we can account for the unobserved reactions by
this argument.

E. K*Δ Cross-sections

In figure 9 we show plots of $p\pi^+$ effective mass
versus $K^+\pi^-$ effective mass. The cross-sections for
the reactions

$$K^+p \to K^{*0}\Delta^{++}$$
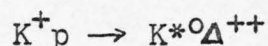
have been determined by the method described in
appendix I. These are shown in table 10 along with
the total K*Δ cross-section.

In figure 10 we present all available data for K*Δ
production up to 2.5 GeV/c, along with the $KN\pi\pi$ cross-

a.
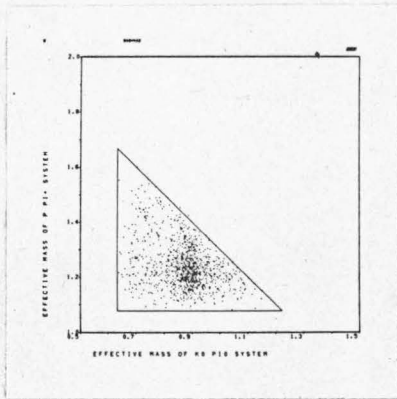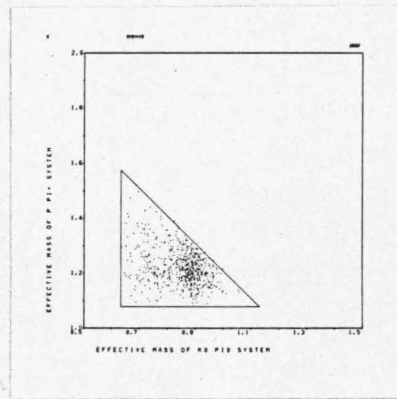
b.
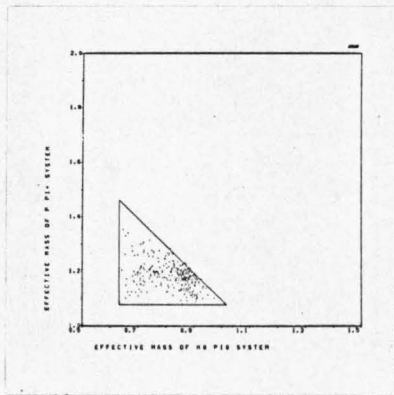
c.
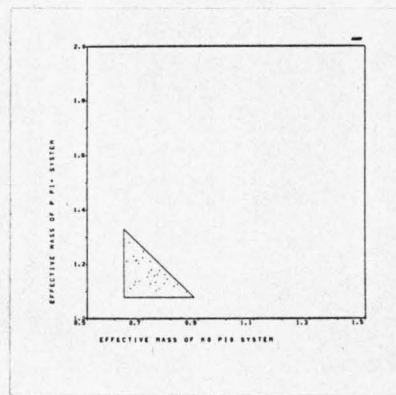
d.

Figure 9. Effective Mass Plots for the Reaction
$K^+p \rightarrow pK^+\pi^+\pi^-$ at four momenta: a.) 2.17 GeV/c
b.) 1.94 GeV/c   c.) 1.67 GeV/c   d.) 1.37 GeV/c

TABLE 10

CROSS-SECTION FOR K*Δ PRODUCTION

momentum GeV/c	$(K^+p \rightarrow K^{*0}\Delta^{++})$ mb.	$(K^+p \rightarrow K^*\Delta)$ mb.
2.17	.77 ± .12	1.53 ± .23
2.07	.61 ± .09	1.21 ± .18
1.94	.59 ± .09	1.18 ± .18
1.81	.49 ± .08	.97 ± .15
1.67	.29 ± .04	.57 ± .08
1.52	.06 ± .04	.12 ± .08
1.37	0.	0.
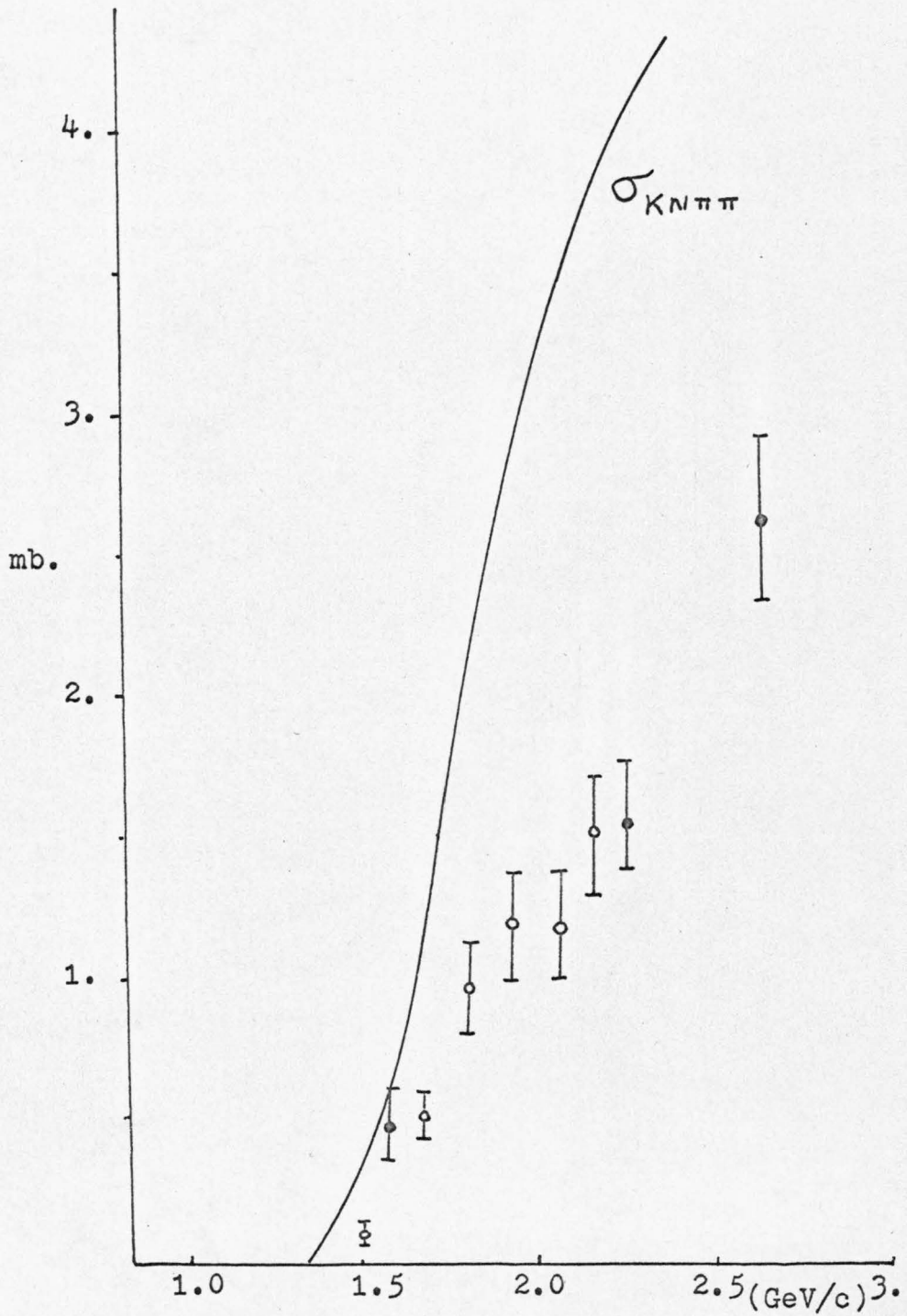
Figure 10. Cross-sections for K*Δ Production.
Open symbols refer to this experiment, solid to
reference 11.

section from figure 6. Again we see that the two pion production is related to the production of the K*Δ state. Throughout the momentum range studied, K*Δ production accounts for about 50% of the KNππ final state.

F. K⁺p Total Cross-section

We began our study of the K⁺p reactions to investigate the structure observed in the total cross-sections. It is interesting, then, to see how the features of the total cross-section are related to the cross-sections for single pion and two pion procuction.

In figure 11 we show once again the KNπ and KNππ cross-sections. We also include the elastic cross-section from figure 1. The sum of the three curves is shown at the top, and is compared with the measured total cross-section data. The curve reproduces the measured cross-sections very well, and seems to account for the features observed earlier.

The first bump in the total cross-section appears to be associated with the rapid rise of the KNπ cross-section. This has been studied in more detail by Bland et al.[5] who found no evidence for a resonance in this momentum range. They conclude that the structure is due entirely to the onset of the
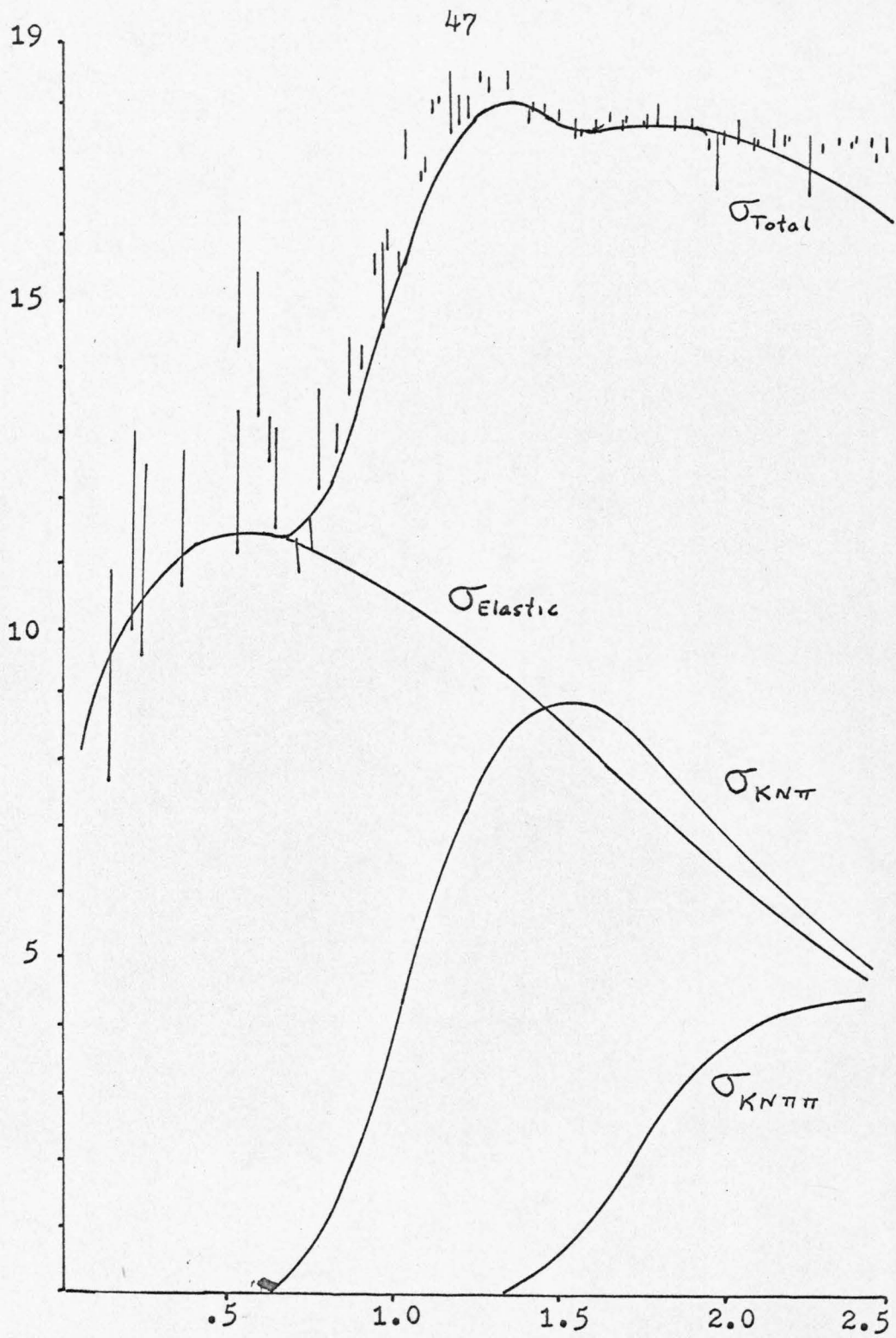
Figure 11. K⁺p Partial Cross-sections.

inelastic channels.

The second bump in the total cross-section appears just above the rapid rise of the $KN\pi\pi$ cross-section. It is tempting to conclude that this feature is also related to inelastic thresholds. This possibility will be considered in the remainder of this paper.

VII. PRODUCTION AND DECAY ANGULAR DISTRIBUTIONS

A. General Discussion

The production and decay of resonances in
quasi-two body reactions can provide very useful
information about the reaction mechanism for the
process. In the case of the reactions studied in
this experiment, considerable information has
already been accumulated at higher energies, showing
the dominance of peripheral mechanisms. The data
of Bland on single pion production shows the
dominance of exchange processes at momenta down to
threshold.

The dominance of peripheral mechanisms is
not, however, inconsistent with the existance of
direct channel resonances. The two descriptions
are, in fact, complementary, and are related in
an average way by finite energy sum rules. The
presence of a Z^*, then, would give some local
variation about the average contribution from the
perpheral mechanism. Such an effect is already
known to be small and is very difficult to analyse
quantitatively.

The data on reactions where resonances are known to be important can serve as guidelines in our discussion of the K^+p scattering. For example the reaction

$$\pi^+ p \to \pi^\circ \Delta^{++}$$
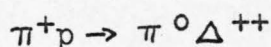
is analogous to our reaction

$$K^+ p \to K^\circ \Delta^{++}$$
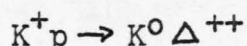
This reaction has been studied over approximately the same momentum range as this experiment[12]. The differential cross-section shows a very striking effect from the dominant $F_{37}(1950)$ partial wave at momenta about 1.5 GeV/c. A Legendre polynomial fit has been made to the angular distribution and shows that the coefficient A_6 becomes large and negative in this range. The odd coefficients A_5 and A_7 change sign at about 1.5 GeV/c, indicating a rapid phase change in the dominant amplitude.

This resonance is known from elastic phase shift analysis. It has a rather large elasticity (.4), and the branching fraction into $\pi\Delta$ is about 50%. In addition the high spin enhances the effect both because of the factor $(J+\frac{1}{2})$ and because the contribution to the Legendre expansion is in the

highest order terms. The effect of higher partial waves appears to be negligible at these energies.

It is much more difficult to see the effect of resonances in lower partial waves. Since any partial wave (angular momentum L) contributes to the Legendre coefficients of order 2L and less, a good knowledge of the highest partial waves is required to separate the effect of any lower wave. This information has come from the phase shift analysis of the elastic scattering data[13].

The Kp system in this momentum range is very similar kinematically to the πp case, and allows the same partial waves. The best candidate for a Z*, however, is the P_{13} partial wave. These facts make it impossible to answer the question of the existance of the Z*. The knowledge of the inelastic differential cross-sections can, however, provide additional constraints for the partial wave analysis of elastic differential cross-sections and polarizations, and should help reduce the number of ambiguous solutions.

In the next sections, we will consider in turn each of the quasi-two body channels.

We will use the normalized Legendre expansion
coefficients to describe the differential cross-
section at each momentum. This, combined with
the data of Bland[5], will provide a complete, and
model independent description of the inelastic
channels from threshold to 2.2 GeV/c. All suggested
resonance phenomena are within this range.

The remainder of the discussion will be in
terms of the exchange model description. Using
the spin density matrix elements we can compare
our data with data at higher momenta, and can
study in a qualitative way the mechanisms in each
of the quasi-two body channels.

B. $K^0 \Delta^{++}$ Differential Cross-section

The qualitative features of the production
angular distribution are shown in figure 12 where
Θ_{cM} is the angle of the Δ measured with respect
to the incident proton in the production center
of mass. As expected, the reaction is strongly
peaked in the forward direction. This peaking
becomes more pronounced as the energy increases.

A quantitative measure of these effects is
shown by the energy dependence of the normalized
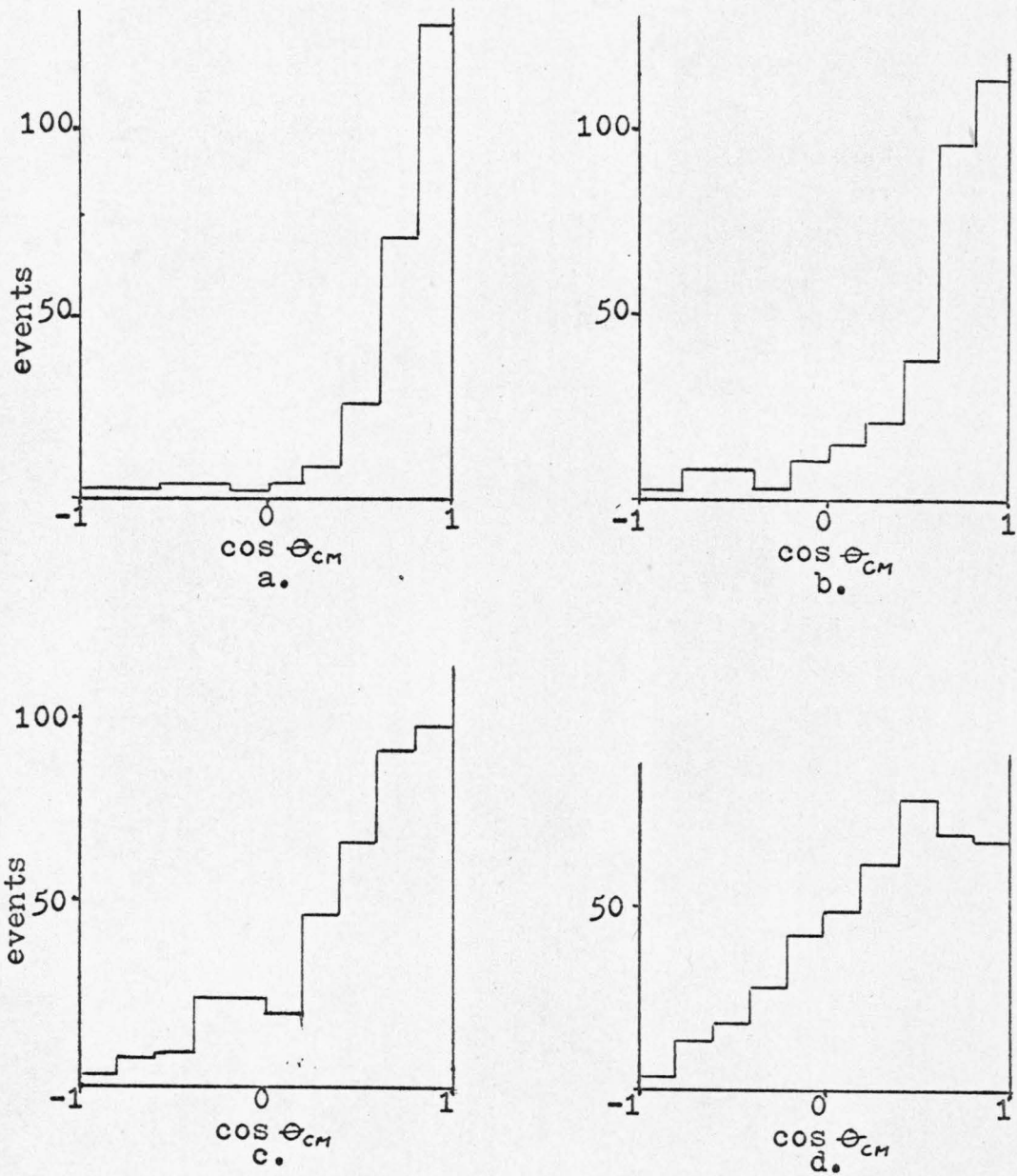
Figure 12 . Δ Production Angular Distributions
at four incident momenta: a. 2.17 GeV/c , b. 1.94 GeV/c ,
c. 1.67 GeV/c , d. 1.37 GeV/c

Legendre coefficients.

$$W (\cos \Theta_{CM}) = 1 + \sum_{\ell} A_{\ell} \, P_{\ell} \, (\cos \Theta_{CM})$$

These are shown in table 11 for the momenta of this experiment. The behavior of the first four coefficients from threshold to 2.17 GeV/c is shown in figure 13.

The region up to 1.58 GeV/c has been studied by Bland et al[5] and the Δ production and decay were found to be in good agreement with the predictions of the rho-photon analogy of Stodolsky and Sakurai[14]. In particular, the production distribution shows a $\sin^2 \Theta_{CM}$ dependence corresponding to $A_2 = -1$. At higher momenta, the reaction becomes more peripheral as other partial waves become important.

The data from this experiment is in good agreement with that of Bland over the range of overlap, and show a smooth variation with incident momentum.

It has been pointed out by Bland that the simple rho-photon analogy fails to explain the magnitude or energy dependence of the differential

TABLE 11

LEGENDRE COEFFICIENTS FOR $K^0 \Delta^{++}$ PRODUCTION

momentum GeV/c

	1.37	1.52	1.67	1.81	1.94	2.07	2.17
A_1	.97±.06	1.19±.06	1.40±.07	1.52±.07	1.72±.07	1.77±.08	2.03±.07
A_2	-.22 .10	.22 .09	.51 .11	.83 .12	1.19 .11	1.44 .15	1.97 .12
A_3	-.37 .12	-.19 .11	-.07 .13	.06 .15	.17 .14	,76 .19	1.03 .18
A_4	-.30 .13	-.46 .12	-.57 .14	-.36 .16	-.76 .16	.05 .21	-.14 .21
A_5	-.09 .15	-.59 .14	-.77 .17	-.18 .17	-1.09 .17	-.22 .24	-.74 .23
A_6	-.17 .17	-.23 .15	-.39 .19	-.10 .19	-1.35 .19	-.52 .25	-.76 .25
A_7	-.16 .18	.04 .16	-.27 .19	-.24 .20	-1.00 .21	-.65 .29	-.56 .27
A_8	-.11 .19	-.13 .17	-.29 .20	-.44 .22	-.35 .24	-.66 .29	-4.0 .29
A_9	-.19 .20	.04 .19	-.03 .21	-.55 .23	-.11 .25	-.48 .30	-.05 .30
A_{10}	.02 .21	.15 .19	.53 .24	.47 .25	.01 .27	-.29 .32	-.02 .33
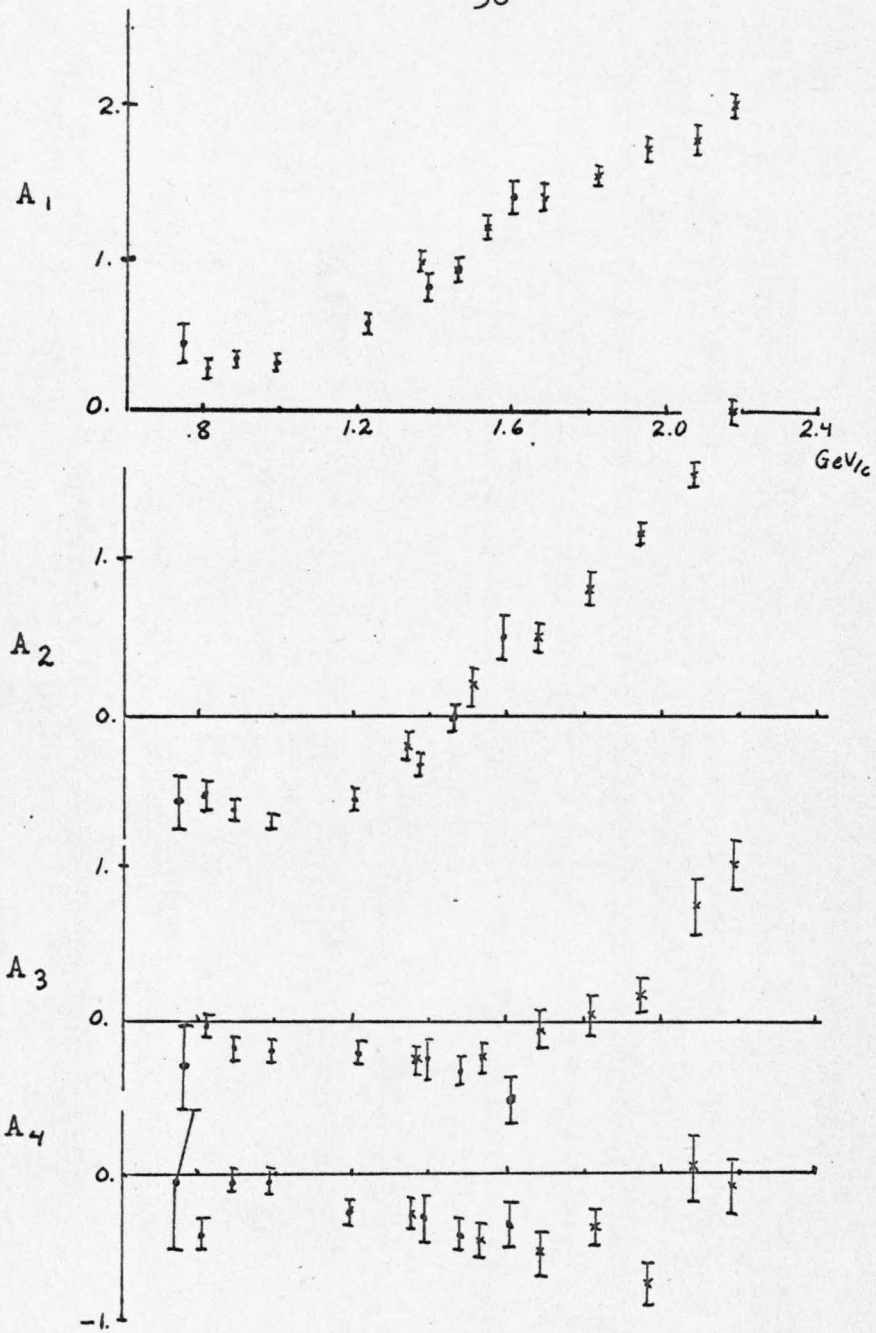
Figure 13. Legendre Expansion Coefficients for the Reaction $K^+p \rightarrow K^0 \Delta^{++}$.

cross-section. The data requires very large
coupling constants, and the reaction becomes
more peripherial faster than predicted from the
simple ρ exchange hypothesis. The data at higher
momenta[15] show a sharp forward peak, explained
by absorption of low partial waves, or by a Regge
model.

The differential cross-sections shown in
figure 14 show a smooth variation with energy.
All momenta show approximately an exponential
dependence with an increasing slope. This behavior
is confirmed by measurements at higher momenta.
The statistics of the experiment are not sufficient
to permit a meaningful comparison with possible
exchange models. In the next section, however,
we will consider the relation of the exchange
mechanism to the decay angular distribution.

C. Δ Decay Angular Distribution

We describe the decay of the Δ in the Gottfreid-
Jackson coordinate frame. The characteristics,
shown in figure 15, appear to be independent of
momentum.
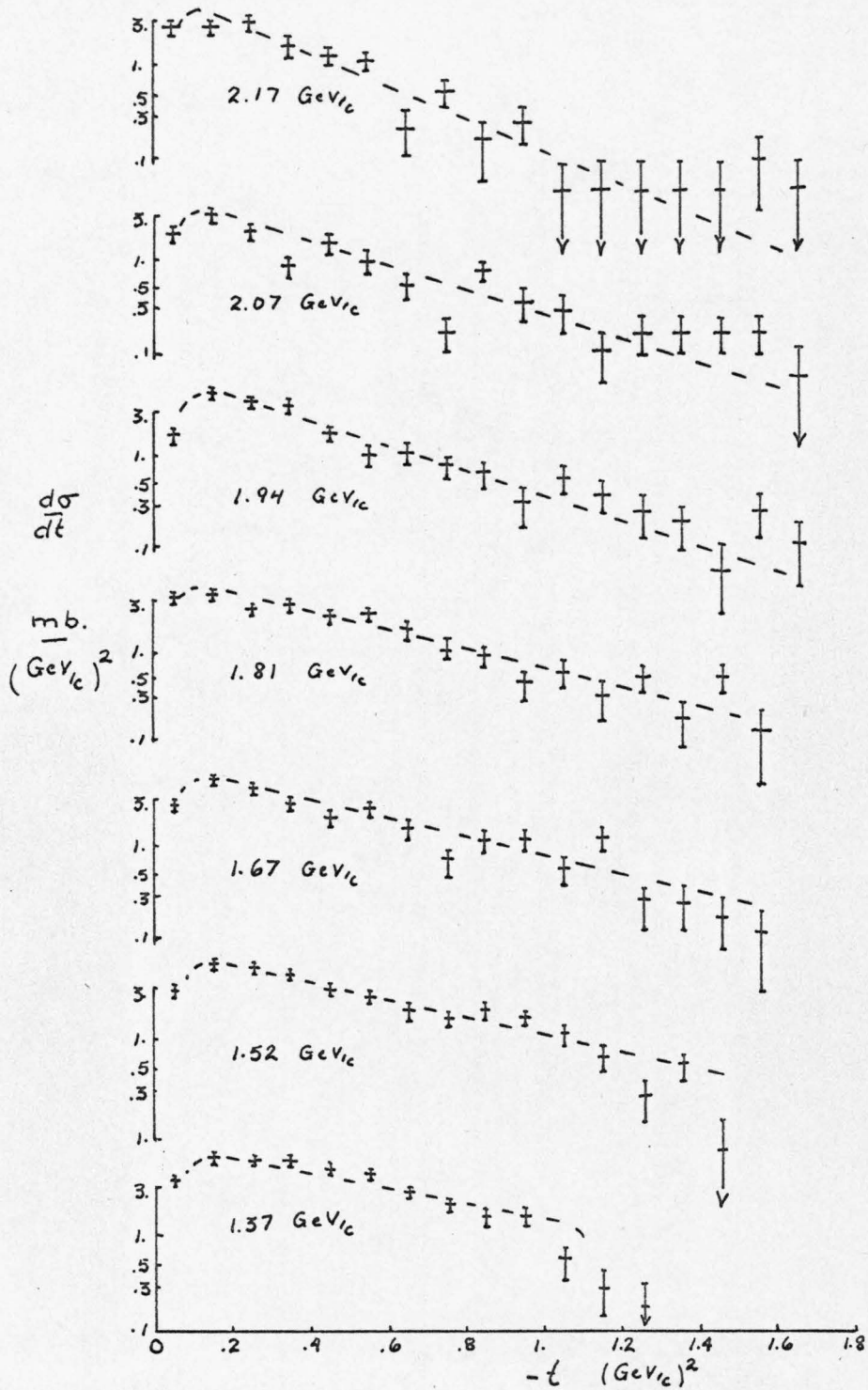
Figure 14. Differential Cross-sections for $K^+p \to K^0\Delta^{++}$
The curves are to aid the eye.
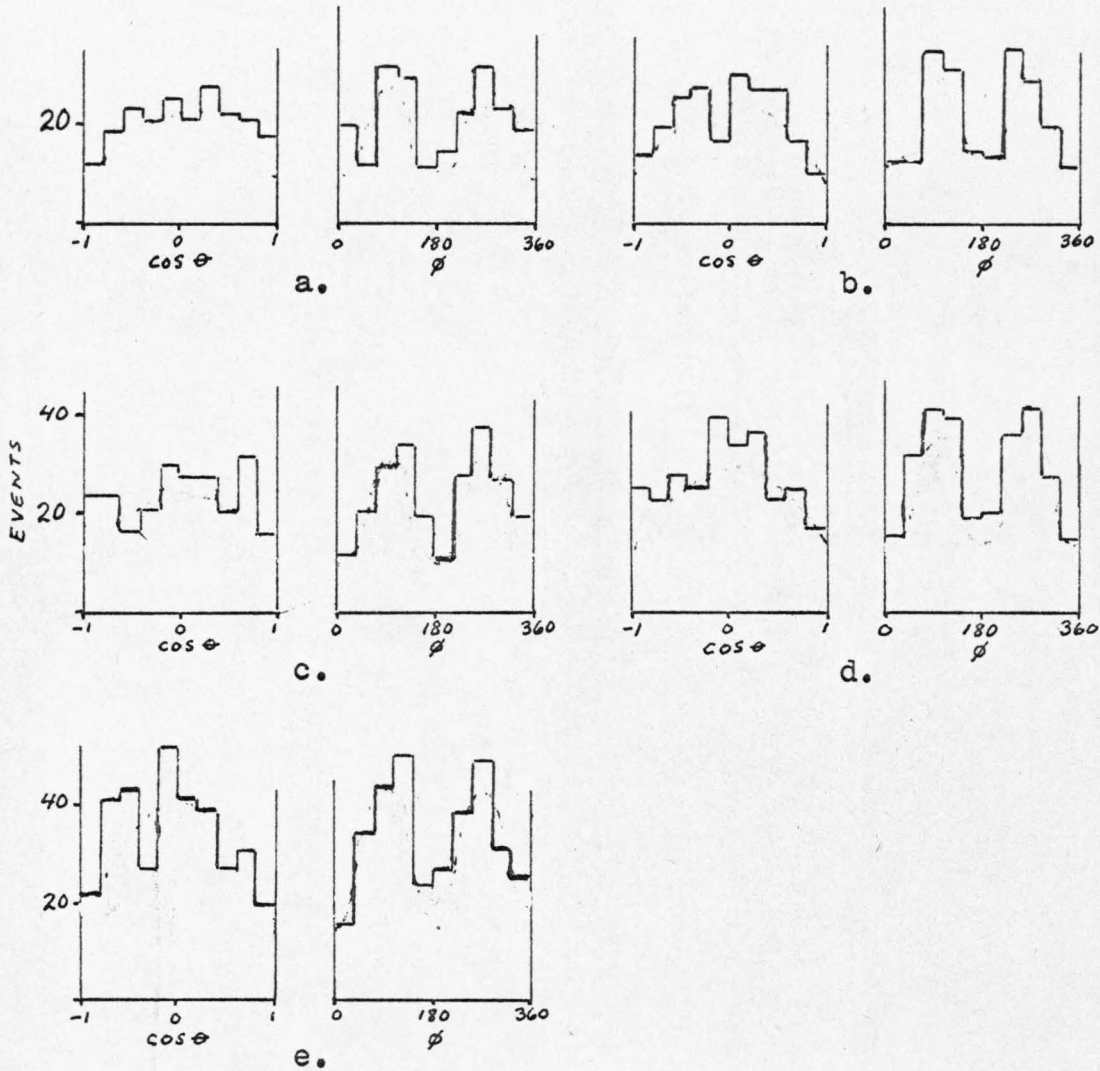
Figure 15. Decay Angular Distributions for the
Reaction $K^+p \rightarrow K^0 \Delta^{++}$ at five momenta: a. 2.17 GeV/c,
b. 2.07 GeV/c, c. 1.94 GeV/c, d. 1.81 GeV/c,
e. 1.37 GeV/c.

To analyse the momentum dependence in detail, we parameterize the distribution by the spin 3/2 density matrix elements. The angular distribution then is given by

$$W(\cos\theta, \phi) = \frac{3}{4\pi}\left[\rho_{33}\sin + \rho_{11}(1/3 + \cos^2\theta)\right.$$
$$-\frac{2}{\sqrt{3}}\text{Re }\rho_{3-1}\sin^2\theta \cos2\phi$$
$$\left.-\frac{2}{\sqrt{3}}\text{Re }\rho_{31}\sin2\theta \cos\phi\right]$$

where $\rho_{33} = \frac{1}{2} - \rho_{11}$

The values of the density matrix elements have been evaluated from the moments of the angular distribution. The results are shown in table 12 and are compared, in figure 16, with data at other momenta[10].

As mentioned previously, the rho-photon analogy of Stodolsky-Sakurai[14] provides a simple description of the $N\rho\Delta$ coupling. They suggest that the ρ exchange reactions

$$\pi^+p \to \pi^0\Delta^{++}$$
$$K^+p \to K^0\Delta^{++}$$
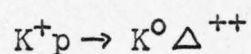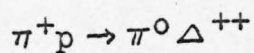
have the same features as Δ photoproduction which

TABLE 12

Δ^{++} DENSITY MATRIX ELEMENTS

momentum	ρ_{33}	Re ρ_{3-1}	Re ρ_{31}
1.37	.379±.027	.230±.031	.059±.025
1.52	.365 .028	.127 .030	.074 .026
1.67	.278 .032	.122 .031	.015 .033
1.81	.329 .032	.245 .032	.016 .027
1.94	.232 .037	.208 .033	.069 .031
2.07	.319 .035	.279 .034	-.033 .031
2.17	.314 .036	.179 .037	.004 .034
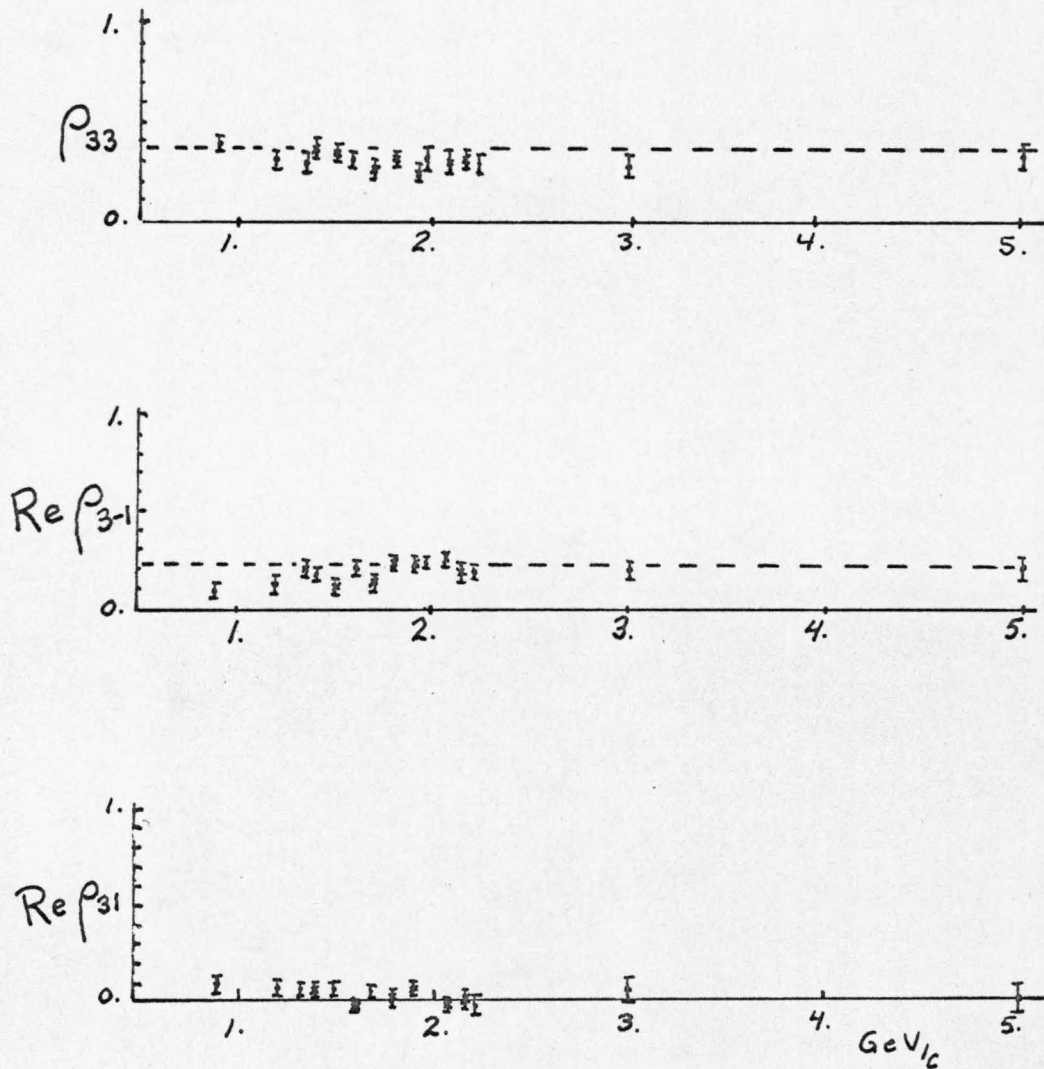
Figure 16. Δ^{++} Density Matrix Elements.
The dotted line corresponds to the M1 prediction
of Stodolsky-Sakurai discussed in the text.

is known to be dominated by an M1 transition.
The rho-photon analogy then predicts a decay angular
distribution

$$W(\cos\theta, \phi) = \frac{1}{16\pi}\left\{ 2 + 3 \sin^2\theta - 3 \sin^2\theta \cos2\phi \right\}$$

In terms of the density matrix elements, the
Stodolsky-Sakurai predictions are

$$\rho_{33} = 3/8 = .375$$
$$\mathrm{Re}\ \rho_{3-1} = \sqrt{\frac{3}{8}} = .218$$
$$\mathrm{Re}\ \rho_{31} = 0.$$

These values are shown in figure 16 and
appear to be in good agreement with experiment
over a wide range of incident momentum.

This result is actually more general than
simple exchange. In contrast to the case of
$\pi^0 \Delta^{++}$ production, which allows only ρ exchange,
the $K^0 \Delta^{++}$ state can also be formed by exchange of
the A_2. An analysis[16] of the complementary
reaction

$$\pi^+ p \to \eta \Delta^{++}$$
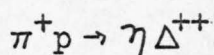
which allows only A_2 exchange, also appears to be

consistent with the predictions of M1 dominance.

The data at higher momenta[15] do show a deviation from the simple M1 predictions for $|t| \lesssim .1$ $(GeV/c)^2$. We have found no consistent variation of the density matrix elements with momentum transfer. However, because of the kinematic cut off in t, we cannot determine values for $|t| < .1$.

D. K*p Differential Cross-section

The production angular distributions for the reaction

$$K^+p \to K^{*+}p$$
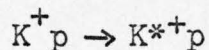
show the same qualitative features as previously described for the $K^o \Delta^{++}$ production. The coefficients of the Legendre expansion are given in table 13. In figure 17 we summarize the energy dependence of the production angular distribution from threshold to 2.17 GeV/c. The data confirm the smooth behavior and the increasingly peripheral nature of the reaction.

The differential cross-sections shown in figure 18 suggest an approximately exponential

TABLE 13

LEGENDRE COEFFICIENTS FOR K*⁺p PRODUCTION

momentum GeV/c

	1.37	1.52	1.67	1.81	1.94	2.07	2.17
A_1	.89±.09	1.16±.07	1.10±.08	1.42±.08·	1.64±.08	1.49±.10	1.82±.08
A_2	.16 .12	.48 .11	.50 .12	.89 .14	1.27 .14	1.01 .15	1.63 .15
A_3	.04 .15	.12 .13	.17 .15	.35 .17	.66 .17	.49 .19	.85 .20
A_4	-.30 .16	-.24 .15	-.07 .17	.01 .18	.08 .20	-.14 .24	.24 .24
A_5	-.14 .18	-.36 .16	.04 .19	-.16 .10	-.15 .22	-.46 .26	-.26 .26
A_6	.23 .20	-.30 .18	.15 .20	-.17 .22	-.32 .25	-.17 .28	-.26 .28
A_7	.05 .21	.10 .19	.22 .22	-.21 .24	-.18 .27	.22 .30	.12 .31
A_8	-.08 .23	.23 .21	.19 .22	-.34 .26	.00 .28	.39 .32	-.02 .33
A_9	-.10 .24	.01 .22	-.18 .24	-.34 .27	.03 .30	.81 .34	.03 .35
A_{10}	-.22 .26	-.09 .23	0 .26	-.61 .28	.15 .32	.65 .34	-.15 .38
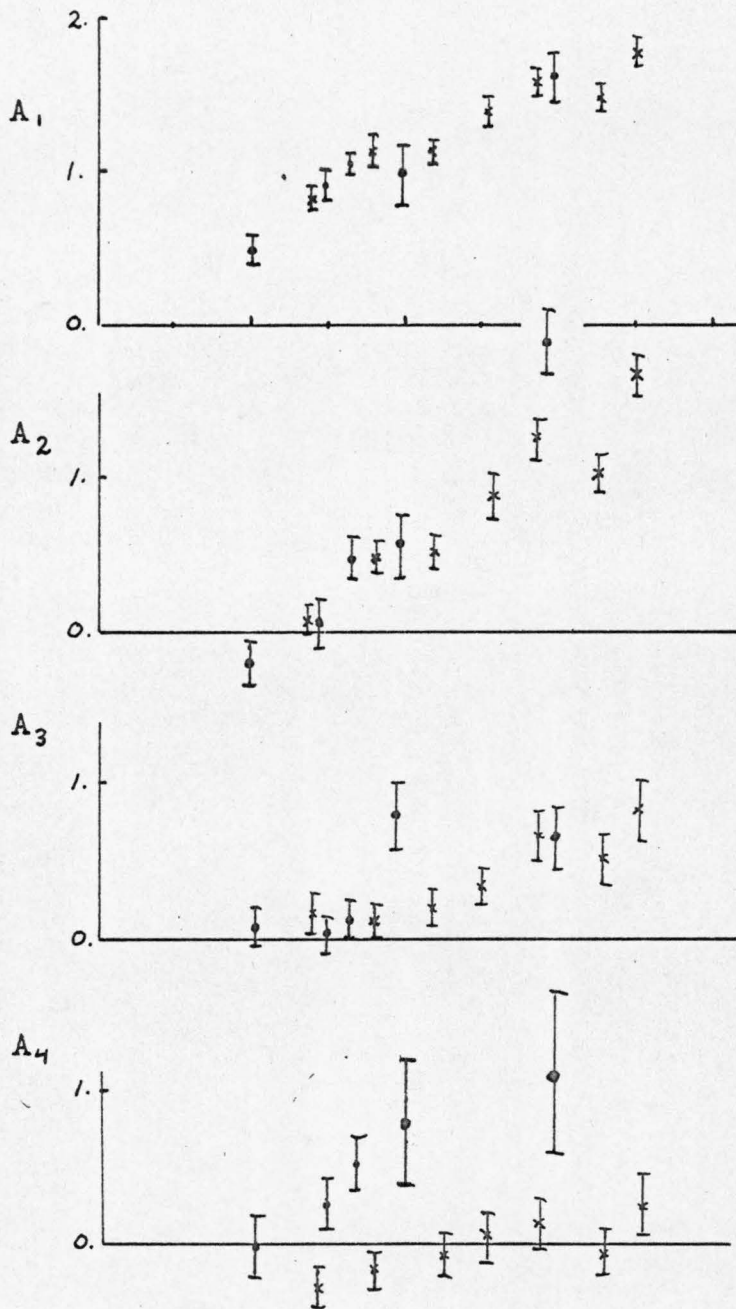
Figure 17. Legendre Expansion Coefficients for
the Reaction $K^+p \rightarrow K^{*+}p$.
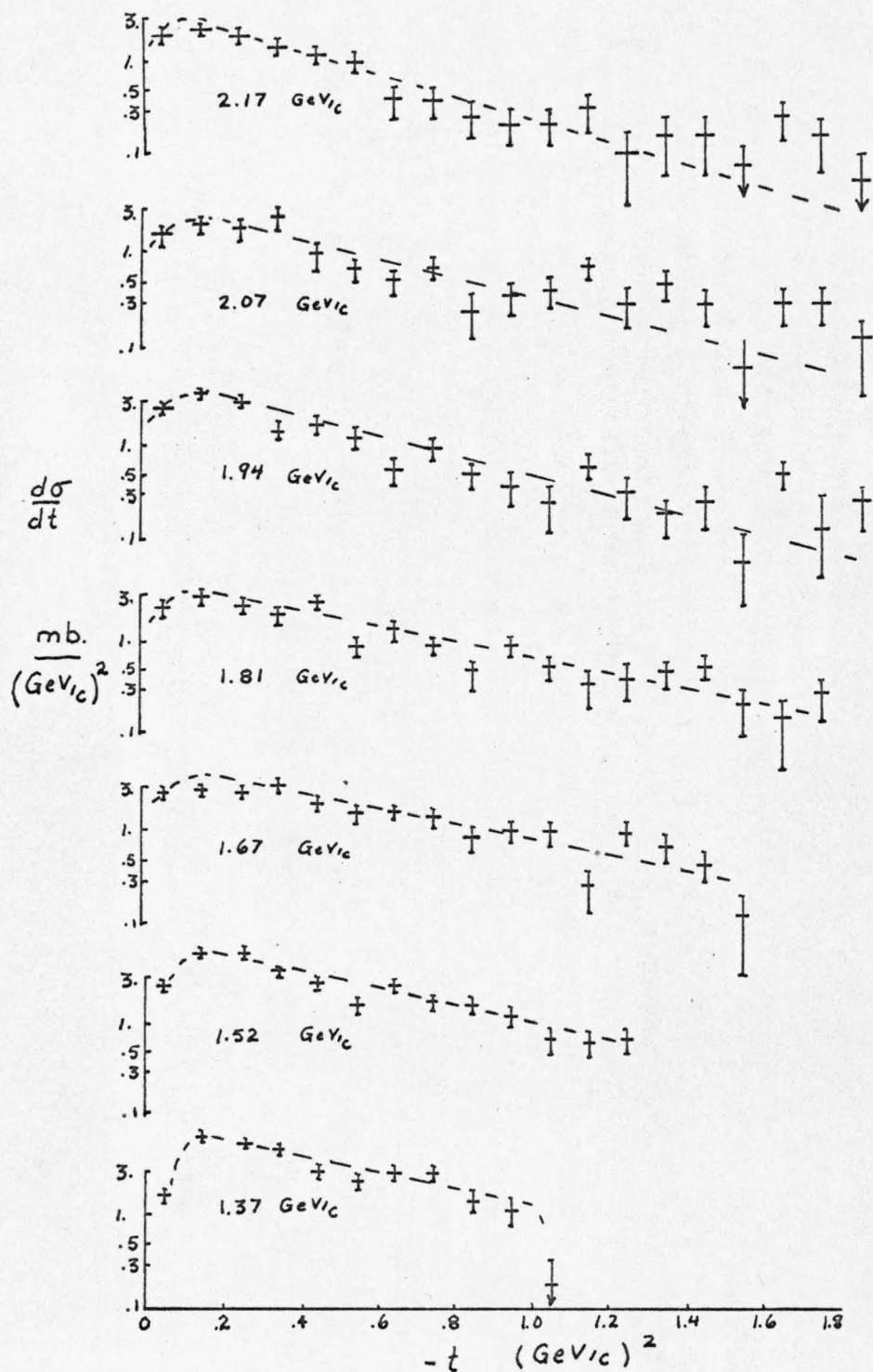
Figure 18. Differential Cross-section for $K^+p \rightarrow K^{*+}p$
The curves are to guide the eye.

dependence on momentum transfer. The slope increases
with energy, in agreement with observations at
higher momentum[15].

The details of this reaction are more com-
plicated than the $K^o \Delta^{++}$ production since both
natural and unnatural parity exchanges are allowed
by angular momentum-parity conservation. The
analysis of data at higher momentum[15] has shown
the dominant contribution to be from π and ω
exchange. The statistics of this experiment are
not sufficiently good to permit a detailed study
of predictions from exchange models. In the
next section, however, we will study the relative
contribution of the exchanges over the momenta of
this experiment.

E. $\underline{K^{*+}}$ $\underline{Decay\ Angular\ Distribution}$

The general features of the K* decay (figure
19) are also very similar to the Δ decay. We
again measure the angles in the Gottfreid-Jackson
frame, defined now by the incoming K^+, and we
parameterize the angular distribution in terms
of the spin 1 density matrix elements.
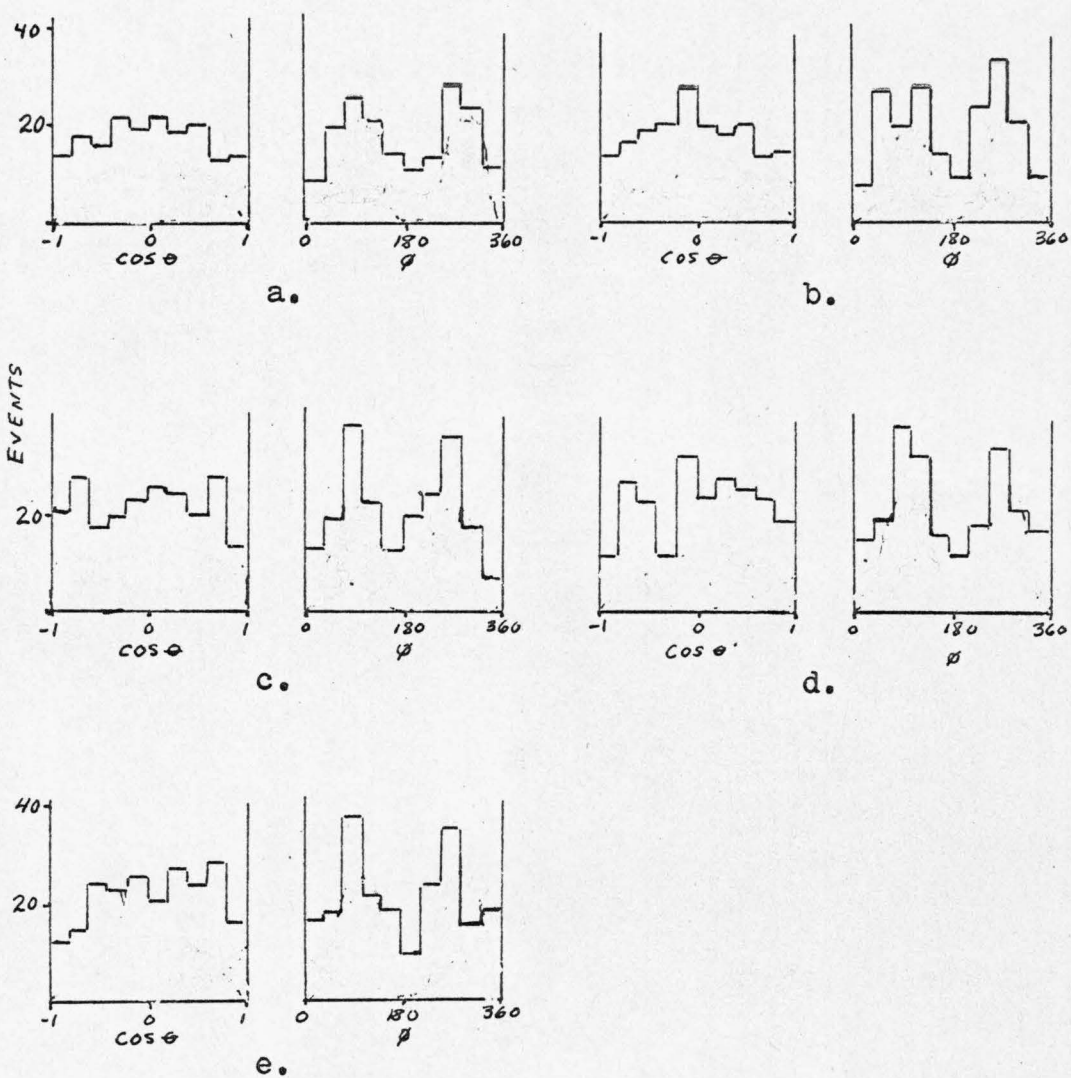
Figure 19. Decay Angular Distributions for the
Reaction $K^+p \rightarrow K^{*+}p$ at five momenta: a. 2.17 GeV/c,
b. 2.07 GeV/c, c. 1.94 GeV/c, d. 1.81 GeV/c,
e. 1.37 GeV/c.

$$W(\cos\theta, \phi) = \frac{3}{4\pi} \left[\rho_{oo} \cos^2\theta + \rho_{11} \sin^2\theta - \rho_{1-1} \sin^2\theta \cos 2\phi \right.$$
$$\left. - \sqrt{2} \, \text{Re} \, \rho_{10} \sin 2\theta \cos\phi \right]$$

with $\rho_{11} = \frac{1}{2}(1 - \rho_{oo})$

The results are given in table 14 for the momenta of the experiment. In figure 20 we show the values of these density matrix elements from threshold to 5 GeV/c. There seems to be very little dependence on momentum over this range.

The two exchange mechanisms, π and ω, mentionned previously contribute to the density matrix elements ρ_{oo} and ρ_{11} respectively. The relative exchange contributions appear to be independent of momentum, in contrast to simple absorption model or Regge predictions. We would expect to see changes particularly at small momentum transfer. However, because of the kinematic cut-off in t our data sample is not sufficient to determine the density matrix elements for low t values.

F. K*Δ Differential Cross-section

The qualitative features of the angular distribution are very similar to those of the

TABLE 14

K* DENSITY MATRIX ELEMENTS

momentum	ρ_{oo}	ρ_{1-1}	Re ρ_{10}
1.37	.163±.039	.169±.044	-.115±.026
1.52	.201 .040	.228 .038	.045 .021
1.67	.141 .042	.230 .040	-.085 .022
1.81	.231 .043	.176 .041	-.051 .027
1.94	.286 .048	.278 .041	-.079 .028
2.07	.203 .047	.215 .042	-.089 .027
2.17	.264 .054	.244 .047	-.075 .027
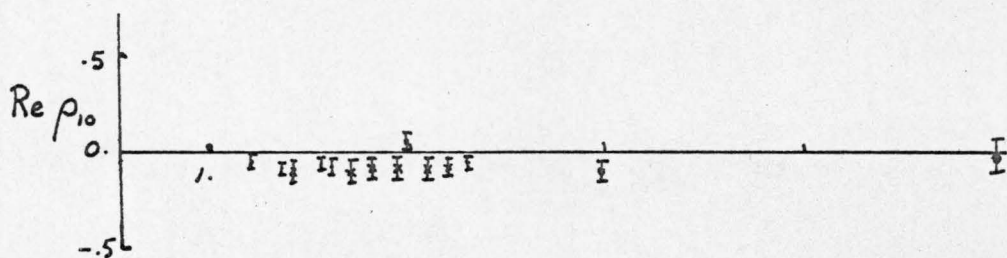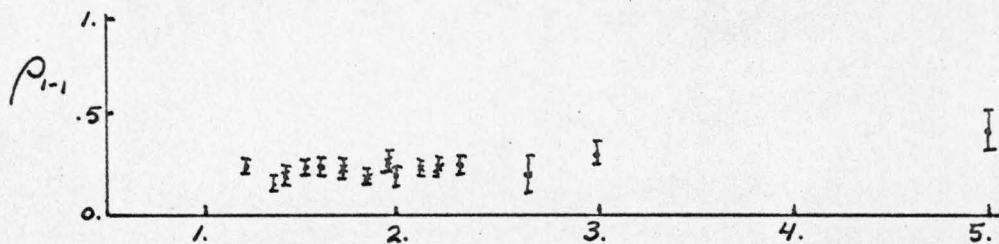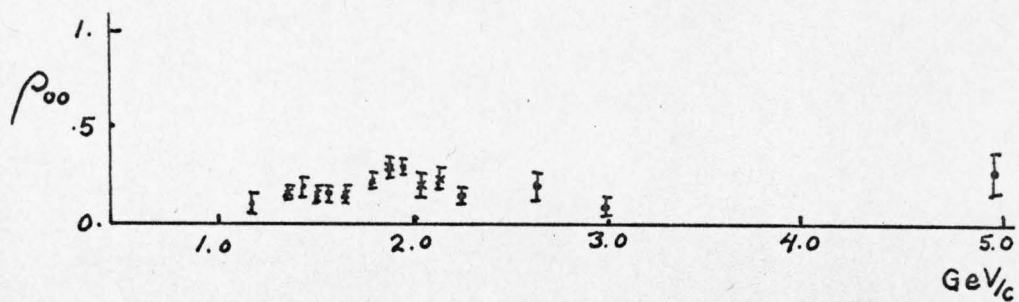
Figure 20. K* Density Matrix Elements.

other channels. This is indicated in the coeffi-
cients of the Legendre expansion shown in table 15,
and in figure 23. The data again show a very smooth
variation, becoming more peripheral at higher
momentum.

The reaction has been studied in detail at
higher momenta and found in reasonable agreement
with models based on π exchange but none of the
models successfully accounts for all the features
of the data[17]. The differential cross-sections
shown in figure 22 provide new information on the
threshold region for this reaction and is quali-
tative agreement with expectations from data at
higher momenta. We have not made a quantitative
comparison with theories but will in the next
section discuss the π exchange interpretation
in connection with the K* and Δ decay.

G. <u>K* and Δ Decay Angular Distributions</u>

The decay cosine and the Treiman-Yang angle
are shown in figure 23. In contrast to the
reactions just studied, there is a very flat dis-
tribution in the Treiman-Yang angle ϕ, consistent

TABLE 15

LEGENDRE COEFFICIENTS FOR $K^{*0}\Delta^{++}$ PRODUCTION

momentum GeV/c

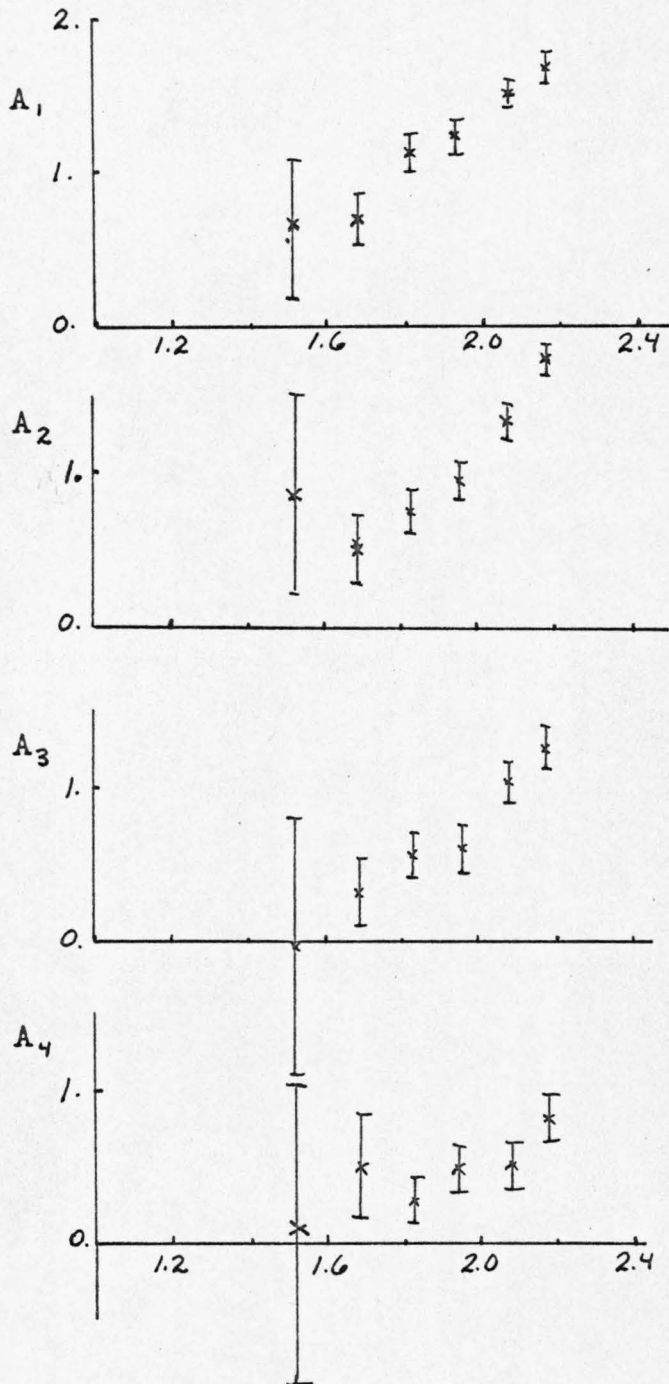|	1.52	1.67	1.81	1.94	2.07	2.17
A_1	.68±.53	.68±.15	1.12±.08	1.24±.07	1.51±.07	1.67±.06
A_2	.93 .66	.60 .20	.77 .12	.98 .11	1.42 .11	1.79 .10
A_3	-.04 .87	.30 .24	.55 .15	.62 .14	1.00 .15	1.23 .13
A_4	.08 .95	.54 .28	.23 .18	.49 .16	.49 .17	.82 .16
A_5	-1.18 1.06	.29 .31	.27 .20	.35 .18	.32 .19	.69 .18
A_6	.66 1.03	-.09 .34	.39 .22	.34 .20	.25 .21	.40 .20
A_7	.72 .89	.27 .36	.40 .23	.20 .22	.24 .22	.28 .22
A_8	-.14 .97	.48 .40	.54 .24	.27 .23	.24 .23	.40 .23
A_9	-1.31 1.24	-.05 .43	.40 .26	.05 .24	.39 .25	.19 .24
A_{10}	.80 1.40	.04 .44	.56 .27	-.08 .24	.23 .26	.21 .24

Figure 21. Legendre Expansion Coefficients for the Reaction $K*p \rightarrow K*^0 \Delta^{++}$.
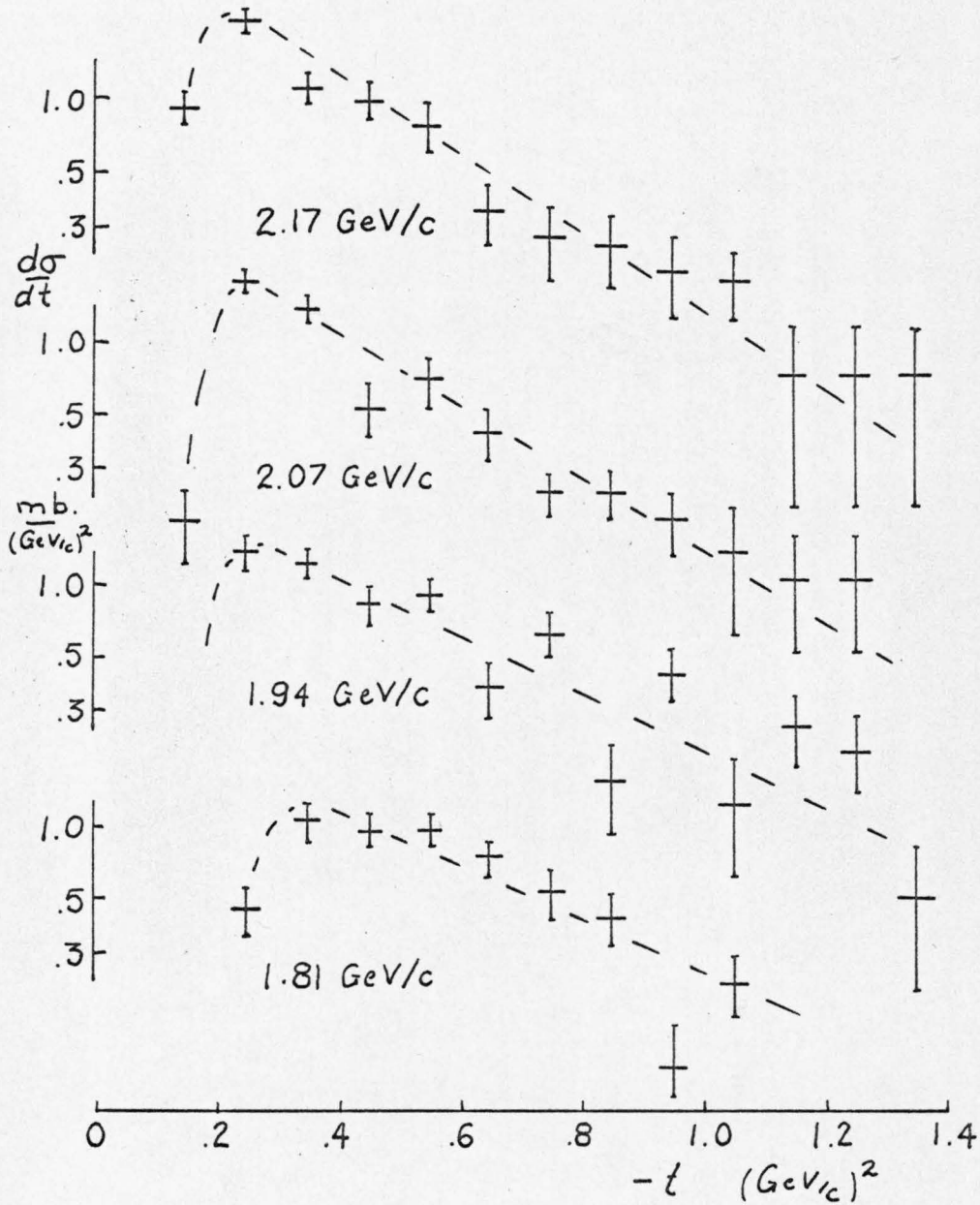
Figure 22. Differential Cross-sections for $K^+p \rightarrow K^*\Delta$
The curves are to aid the eye.
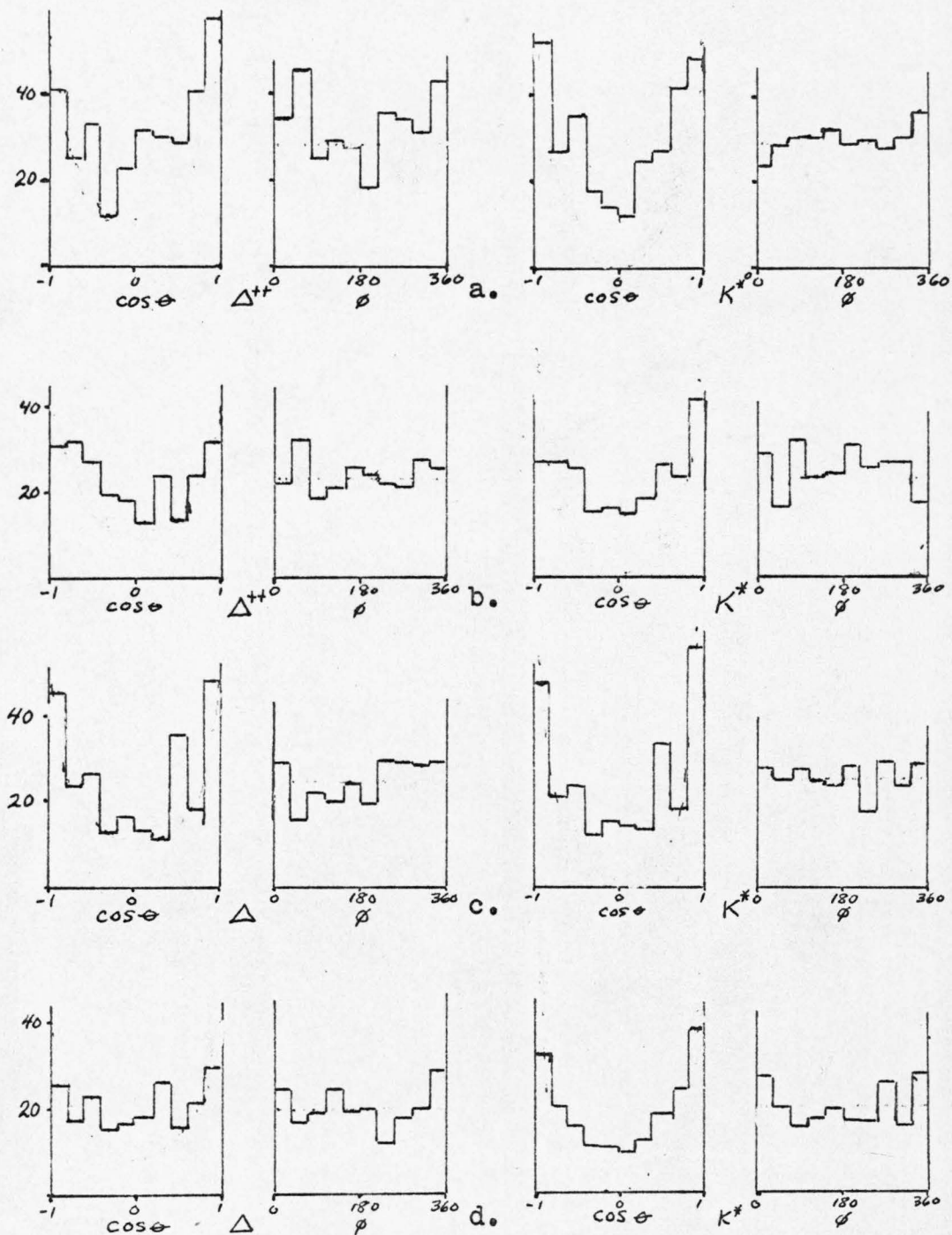
Figure 23. Decay Angular Distributions for the Reaction $K^+p \rightarrow K^{*0} \Delta^{++}$ at four momenta: a. 2.17 GeV/c, b. 2.07 GeV/c, c. 1.94 GeV/c, d. 1.81 GeV/c.

with the dominance of π exchange. This is in agreement with the data at higher momentum[17].

We have determined the density matrix elements for both the K* and Δ (table 16) and compare the results with data at higher momenta in figure 16. The data appear to be rather independent of momentum up to at least 3 GeV/c. The predictions of simple pion exchange can be obtained by ordinary addition of angular momentum. This gives

$$K*: \quad \rho_{oo} = 1. \qquad \rho_{1-1} = 0. \qquad \text{Re}\,\rho_{1o} = 0.$$

$$\Delta: \quad \rho_{33} = 0. \qquad \text{Re}\,\rho_{3-1} = 0. \qquad \text{Re}\,\rho_{31} = 0.$$

The density matrix elements, averaged over momentum transfer, do show a consistent deviation from these predictions. Data at higher momenta show that the predictions are well satisfied for small momentum transfer ($|t| \lesssim .1(\text{GeV/c})^2$) but our data are not sufficient to make any conclusion on this.

TABLE 16

$\triangle$ AND K* DENSITY MATRIX ELEMENTS

momentum	ρ_{33}	Re ρ_{3-1}	Re ρ_{31}	ρ_{00}	ρ_{1-1}	Re ρ_{10}
1.67	.129±.043	-.025±.042	.047±.049	.599±.067	.013±.044	-.030±.037
1.81	.127 .029	-.034 .026	-.012 .029	.659 .040	-.047 .028	-.080 .025
1.94	.158 .027	.014 .024	-.027 .026	.616 .037	.010 .026	-.086 .022
2.07	.139 .028	.037 .025	-.031 .027	.604 .037	.018 .027	-.066 .022
2.17	.099 .025	-.018 .021	-.064 .025	.619 .032	-.030 .024	-.048 .020
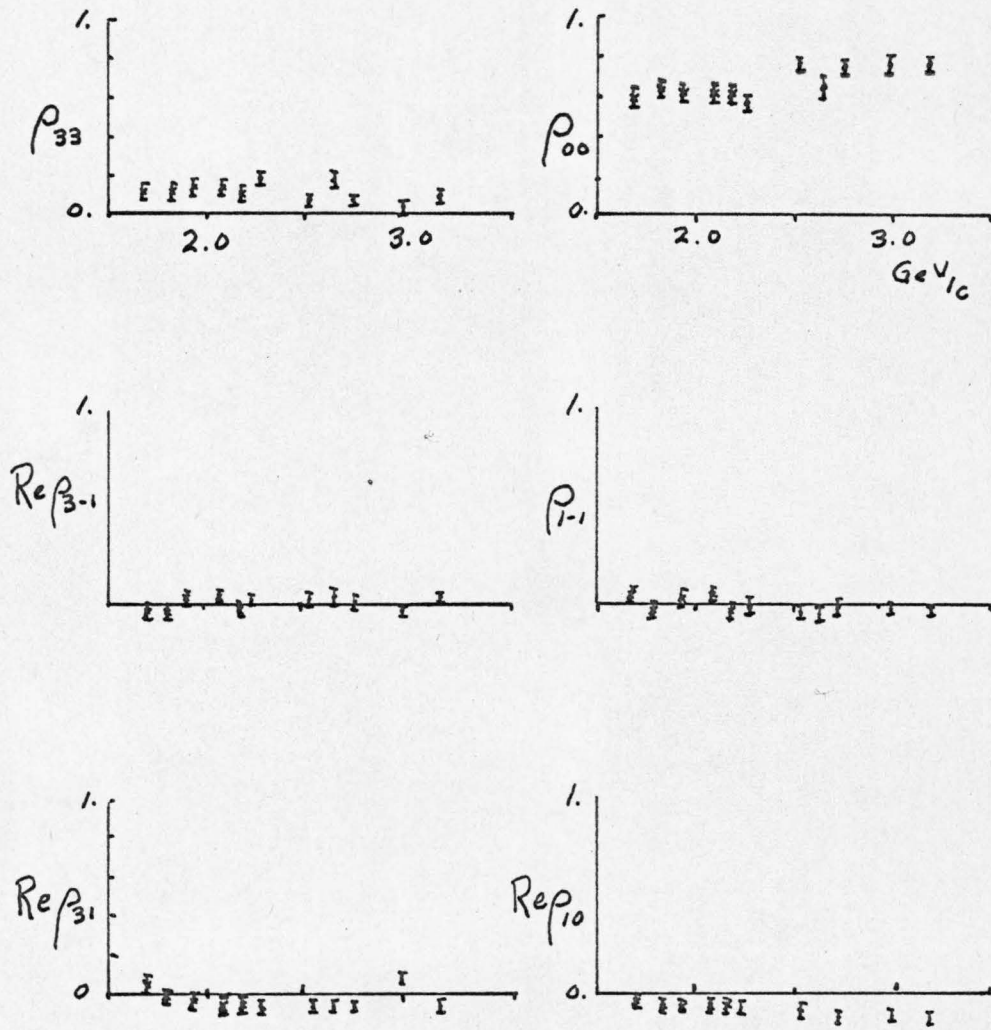
Figure 24. Δ and K* Density Matrix Elements.

H. Quark Model Predictions

Bialas and Zalewski[18] have derived a set
of relations between single particle decay angular
distributions and joint decay distributions for
the reaction

$$K^+ p \rightarrow K^* \Delta$$
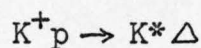
The observable predictions given for decay
distributions are presented as predictions about
tensors formed from the moments of the angular
distributions.

$$T^{20}_{MO} (K^*, \Delta) = \frac{1}{\sqrt{2 \cdot \frac{3}{2} + 1} \; F(K^*)} \left\langle Y^M_2(K^*) \right\rangle$$

$$T^{02}_{OM} (K^*, \Delta) = \frac{1}{\sqrt{2 \cdot 1 + 1} \; F(\Delta)} \left\langle Y^M_2(\Delta) \right\rangle$$

$$T^{22}_{MN} (K^*, \Delta) = \frac{1}{F(K^*) \; F(\Delta)} \left\langle Y^M_2(K^*) Y^N_2(\Delta) \right\rangle$$

$$F(K^*) = -\sqrt{\frac{3}{10\pi}}$$

$$F(\Delta) = -\sqrt{\frac{1}{5\pi}}$$

where $Y^M_2(K^*$ or $\Delta) =$ spherical harmonic evaluated
at K^*, Δ decay angle
and $\langle \; \rangle$ means an average over the decay angular

distribution.

To describe the quark scattering process, there are four independent spin nonflip and four spin flip amplitudes. The particle-particle scattering amplitude is the coherent sum of the constituent quark-quark scattering amplitudes.

The tensors can be written in terms of these amplitudes and if the quantization axis is taken as the production normal, we get the following relations.

I. $\quad T_{oo}^{20}(K^*, \Delta) = \sqrt{2}\; T_{oo}^{02}(K^*, \Delta)$

II. $\quad T_{20}^{22}(K^*, \Delta) = \tfrac{1}{2}\; T_{20}^{20}(K^*, \Delta)$

III. $\quad T_{02}^{22}(K^*, \Delta) = \frac{1}{\sqrt{2}}\; T_{02}^{02}(K^*, \Delta)$

IV. $\quad T_{oo}^{22}(K^*, \Delta) = \frac{1}{2\sqrt{6}} - \frac{1}{\sqrt{2}}\; T_{oo}^{02}(K^*, \Delta)$

Since II and III are in general complex, there are six equations. We have combined all data at four momenta 1,81, 1.94, 2.07 and 2.17 GeV/c. The results are shown in table 17 and indicate rather good agreement. Figure 27 shows a summary of the test of these relations up to 5 GeV/c. The values of the tensors are rather

TABLE 17

TEST OF QUARK SCATTERING RELATIONS
EVALUATED IN THE TRANSVERSE HELICITY FRAME

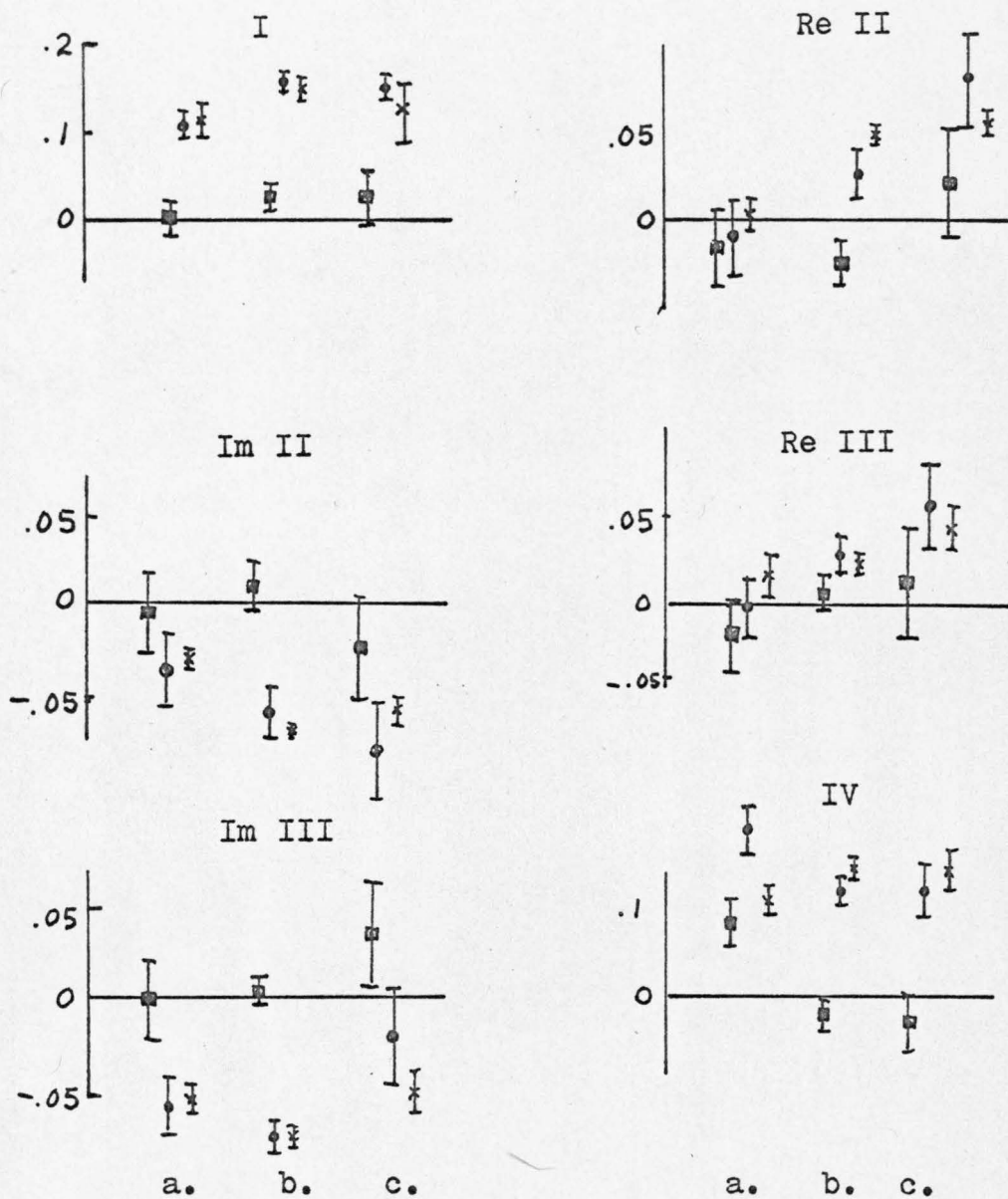| equation	left side	right side	difference
I	.104±.013	.105±.027	-.001±.030
Re II	-.012 .023	.006 .006	-.018 .023
Im II	-.040 .022	-.034 .005	-.006 .023
Re III	.003 .021	.020 .010	-.017 .023
Im III	-.062 .021	-.057 .010	-.005 .024
IV	.177 .029	.100 .018	.077 .034

84

Figure 25. Test of Quark Scattering Relations for three momenta. a) 1.8 - 2.2 GeV/c, this expt. b) 2.5 - 3.2 GeV/c, ref. 17. c) 5.0 GeV/c, ref. 17. The figure shows the difference ∓ , left side ∓ , and right side ∓ .

independent of momentum and in all cases, the
equalities are well satisfied.

VIII. CONCLUSIONS

We have studied single pion production and two pion production in K^+p reactions. We have studied in detail the two reactions

$$K^+p \rightarrow K^0p\,\pi^+$$
$$\rightarrow K^+p\,\pi^+\pi^-$$
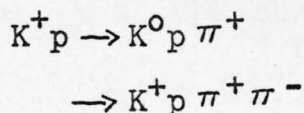
The cross-section for the $K^0p\,\pi^+$ reaction shows a smooth fall off with increasing momentum, as had been suggested previously by Bland[5]. This final state shows strong production of the quasi-two body states $K\Delta$ and K^*N as at lower momenta. There is no evidence of significant interference between these two channels.

The $pK^+\pi^+\pi^-$ cross-section rises rapidly above 1.7 GeV/c, the threshold for $K^*\Delta$ production. About half the events at each momentum correspond to this quasi-two channel. This rapid rise in the two pion production cross-section appears to contribute to the second bump noted in the total cross-section.

We have studied the production angular distribution and decay properties of the quasi-two

body channels. All the observed features are in
agreement with data at higher and lower momenta,
indicating the dominance of peripheral mechanisms.

It is impossible from the inelastic reactions
alone, to place limits on the contribution of
direct channel mechanisms. Our data on quasi-two
body production, however, does provide additional
information on the partial wave structure of the
K^+p interaction, and should be useful in resolving
some of the ambiguities in phase shift analyses
of elastic scattering and polarization data.

APPENDIX

EXTRACTION OF PARAMETERS FOR QUASI-TWO BODY STATES

A. Three Particle Final States

We wish to consider the states $K^o\Delta^{++}$ and K^*p
which decay into the final state $pK^o\pi^+$. The parameters
of interest include the production cross-sections,
possible interference between the K^* and Δ, differential
cross-section for resonance production, and the
resonance decay angular distribution.

A three body state is completely specified by
five variables. We will always take one of these
to be the invariant mass of the system, or equivalently
the beam momentum. The choice for the other parameters
cannot be made so easily, and in the following
discussion we will consider a number of choices
each revealing some different aspects of the reactions.

B. Dalitz Plots

One very useful choice of parameters is the
invariant mass of the two body systems.

In the reaction

$$1 + 2 \rightarrow 3 + 4 + 5$$

we can choose for example

$$M_{34}^2 = (p_3 + p_4)^2$$

$$M_{45}^2 = (p_4 + p_5)^2$$

The third choice is not independent

$$M_{35}^2 = S + M_3^2 + M_4^2 + M_5^2 - M_{34}^2 - M_{45}^2$$

$$S = (p_1 + p_2)^2 = \text{constant}$$

The remaining two variables could be chosen as the polar angles of the plane defined by the three out going particles. For the purposes of this discussion, however, we will average over these angles and consider a plot of M_{45}^2 versus M_{34}^2, suggested first by Dalitz[19].

Figure A.1 shows a number of general features of the Dalitz plot. The boundary corresponds to the limits imposed by energy and momentum conservation. Within this boundary, events should be uniformly distributed if there is no dependence of the reaction amplitudes on the masses of the out going systems. Resonances in the out going systems show up as heavily populated bands in the plot, as shown in the figure for the Δ and K*. In the region I, where the Δ and K* bands cross, we can have events which go through
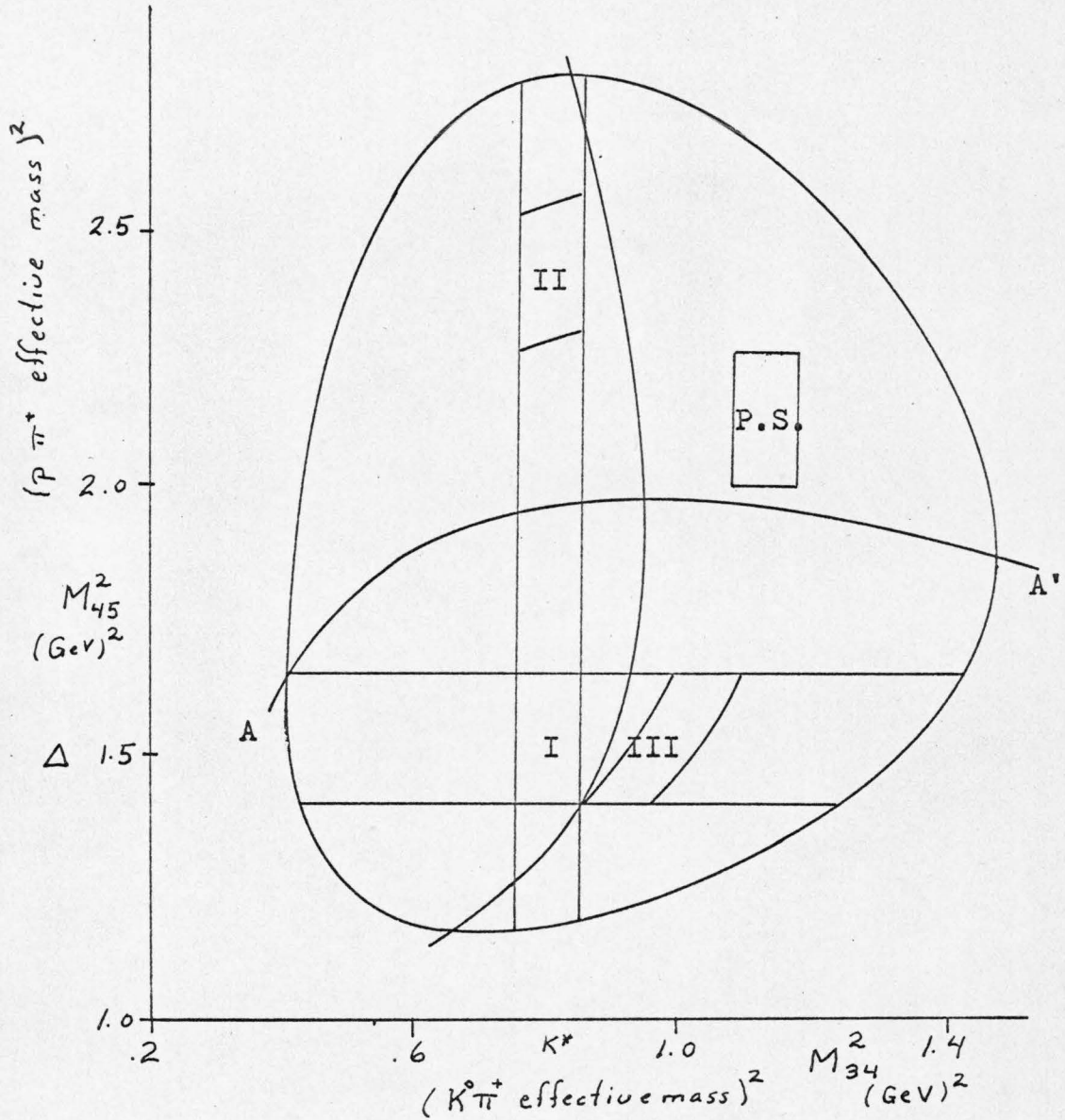
Figure A.1. General Features of Dalitz Plots
The significance of the labled regions is discussed
in the text.

either resonance system, and we must also consider
the interference of these two channels.

C. Mass Conjugation

To study the Δ and K* channels, and the possible
interference, we will use the mass conjugation technique
suggested by Eberhard and Pripstein[20]. For any
effective mass squared for particles 3 and 4, there
is a range of effective mass squared for the system
of particles 4 and 5. This range is given by

$$M^2_{45} = A + B \cos\Theta_4$$

where $\cos\Theta_4$ is the decay cosine of particle 4
measured with respect to the direction of the system
of particles 3 and 4 in the production center of
mass. A and B are constants which depend only on the
total energy and the effective mass M_{34}. The Dalitz
plot limits correspond to $\cos\Theta_4 = \pm 1$ or to $M^2_{45} = A \pm B$,
and the line AA' corresponds to $\cos\Theta_4 = 0$.

The region II shown in figure I.1 is related to
the region I simply by changing the sign of $\cos\Theta_4$,
or by the interchange of particles 3 and 4. For any
resonance of specific parity then, the density of
points in I and in II should be equal, except for
the presence of the resonance in the other two particle

system. In order to get a sample of events in the
M_{34}^2 band, we replace the events in region I by pseudo
events from region II with the two particles 3 and
4 interchanged.

Similarly we can generate pseudo events from the
M_{45}^2 band by taking events from region III and inter-
changing particles 4 and 5. This procedure should
give us a decay angular distribution for one resonant
state without the effect of the other resonance.
To check the validity of the reflection procedure,
we can compare the reflections of regions where the
other resonance does not contribute.

This technique provides a way to extract resonance
decay parameters, without knowing anything about the
reaction in the interference region. It also provides
a method for testing whether there is any interference
between the two reaction channels.

D. Cross-sections and Interference

The mass conjugation technique provides a way
to determine the production cross-sections for
quasi-two body channels in the reaction. We can
simply add up all events in a resonance band, using
events from the conjugate region to fill in the band
where the other resonance, or interference could

be a problem. We then subtract the uniform phase
space background by interpolating between the two
regions outside the resonance band. This has the
advantage that it requires no assumption about the
exact form of the resonant amplitude, or about the
interference of the resonance amplitudes in the region
where the bands cross in the Dalitz plot.

We can also use the technique to determine
whether there is an interference between the two
amplitude. Region II and region III each contain
events from one resonance, plus events from the
phase space distribution, whereas region I contains
events for both resonances, phase space and interference.
The number of events for the phase space distribution
events N_{PS} can be determined from the region where
neither resonance can contribute, so that we can
easily determine the number of events due to inter-
ference effects.

$$N_{INT} = N_I + N_{PS} - (N_{II} + N_{III})$$

We can then calculate an interference cross-
section and determine whether the interference is
constructive or destructive.

E. Four Body Final States

The four body system can be specified by eight parameters. We will always choose one of these to be the total effective mass. In many cases we will choose specific variables of interest and average over all others.

We will consider effective mass distributions as we did for the case of the three body system. For the reaction

$$1 + 2 \rightarrow 3 + 4 + 5 + 6$$

there are many possible choices of effective masses. Since we will be interested in two body resonances, however, we will consider a plot of M_{56} versus M_{34}. We choose here to plot the effective mass rather than effective mass squared, since it makes the calculation of kinematic boundaries slightly simpler.

The range of M_{34} is given by

$$M_3 + M_4 \leq M_{34} \leq E_{cm} - M_5 - M_6$$

where E_{cm} = total energy in center of mass.

For fixed M_{34}, the range of M_{56} is given by

$$M_5 + M_6 \leq M_{56} \leq E_{cm} - M_{34}$$

The boundaries of the plot then form a right triangle, and the effective mass plot will be referred to as a triangle plot.

For the Dalitz plot, we had the result that a constant reaction amplitude gives a uniform density in the plot. There is an analagous result for the triangle plot.

$$N(M_{34}, M_{56}) \, dM_{34} \, dM_{56} = \frac{P_{cm}}{E_{cm}} P_{34} \, P_{56} \, dM_{34} \, dM_{56}$$

where P_{cm} = momentum of M_{34} or M_{56} in the center of mass

P_{34} = momentum of M_3 or M_4 in the M_{34} system

P_{56} = momentum of M_5 or M_6 in the M_{56} system

This given a distribution which varies smoothly over the plot so that resonances in the two particle systems will show up as heavily populated bands.

It is much easier to study the quasi-two channels here, since there is no interference to worry about We can consider all events in the region of the triangle plot where M_{34} and M_{56} are within the region of resonance mass for the K* and Δ. The effect of events from the phase space distribution can be removed by interpolation, as was done in the three body case.

F. Resonance Production Angles

A further specification of the 3 particle or
4 particle system could include the production angle
of a 2 particle resonance in the center of mass.
This choice is independent of the invariant mass
specification considered in the previous section.

For the description of the quasi-two body reactions
in this paper we will always define the production
angle with respect to the incoming particle which
forms the resonance. For Δ production, we measure
with respect to the proton, for K* production, with
respect to the K^{+}.

The choice of production angle is equivalent to
specifying the state by the four momentum transfer
squared.

$$t = (p_{in} - p_{res})^2$$

In the description of the differential cross-
sections for quasi-two body reactions, both of these
descriptions are considered.

G. Resonance Decay Angles

There are two co-ordinate systems in common
use to analyse the decay angular distributions of

resonant states. The Gottfreid-Jackson system or
t-channel frame is shown figure A.2. Here we choose
the positive z axis along the direction of the incoming
proton or K in the Δ or K* center of mass. The
y axis is chosen as the perpendicular to the production
plane, and the x axis is defined by the right hand
rule. The angles of interest are the polar angles
(θ, ϕ) in this co-ordinate system, commonly called
the Jackson angle and Treiman Yang angle respectively.

The other system commonly used is the Helicity
frame shown in figure I.2. The z axis is chosen as
the direction of motion of the resonance in the
production center or mass. The y axis is again the
production normal, and the x axis is defined as
before.

These two co-ordinate systems are parallel
for zero momentum transfer, but are rotated about
the y axis as the momentum transfer increases.

In the case of the three body final state we have
already noted that the decay angle in the Helicity
frame is directly related to the effective mass of
the other two particle system in the Dalitz plot.
In the Jackson frame the relation affects both the
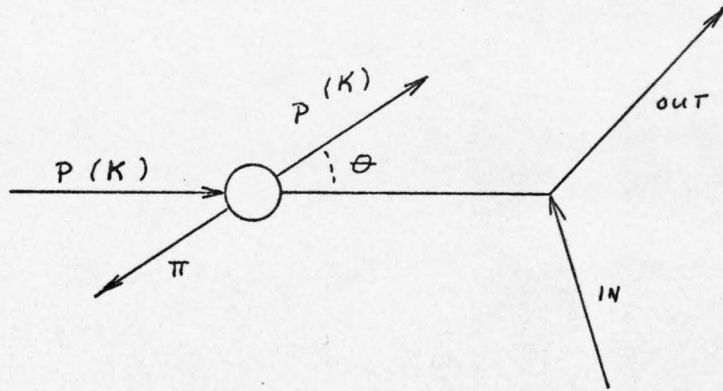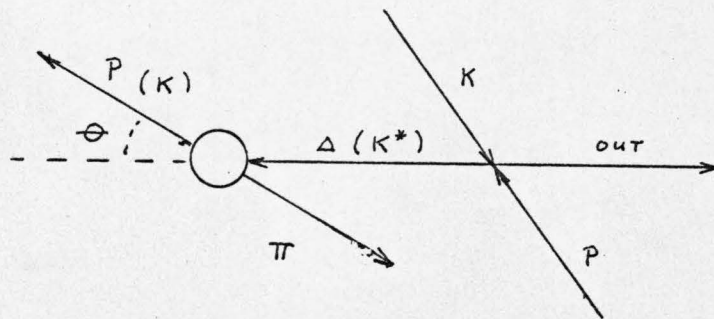
Figure A.2. Decay Co-ordinate Systems
a. Gottfreid-Jackson system for decay of the
△ ,(K*); b. Helicity Frame.

cos θ and ϕ distributions. To eliminate this bias
in all angular distributions we use the mass conjugation
technique already described.

For the four body state, the decay angles are
independent of the effective masses of the resonances,
and we need no such correction.

REFERENCES

1. M. Gell-Mann, Phys. Lett $\underline{8}$, 214 (1964)

   G. Zweig, CERN Report, 1964 (unpublished)

2. R.L. Cool et al., Phys. Rev. Lett $\underline{17}$, 102 (1966)

   R.J. Abrams et al., Phys. Rev. Lett $\underline{19}$, 259 (1967)

   D.V. Bugg et al., Phys. Rev. $\underline{168}$, 1466 (1968)

3. R.W. Bland et al., UCRL 18758, 1968, (unpublished)

   A. Bettini et al., Phys. Lett $\underline{16}$, 83 (1965)

4. S. Kato et al., Phys. Rev. Lett $\underline{24}$,615 (1970)

   P.C. Barber et al., Phys. Lett $\underline{32B}$, 214 (1970)

   F.C. Erne et al., Hyperon Resonances Conference, Duke University, 375 (1970)

5. R.W. Bland, thesis, UCRL 18131, 1968, (unpublished)

6. The beam was designed by J.A. Kadyk of LRL for use at the 25 inch chamber and is described in the Bevatron User's Handbook.

7. F.T. Solmitz et al., Alvarez Group Programming Note P-117 Berkeley, 1965, (unpublished)

8. O.I. Dahl et al., Alvarez Group Programming Note P-126 Berkeley, 1965, (unpublished)

9. O. Dahl, Alvarez Group Programming Note P-124 Berkeley, 1965, (unpublished)

10.   A. Bettini et al., Phys. Lett 16, 83 (1965)

       W. Chinowsky et al., Phys. Rev. 139B, 1411
             (1965)

       F. Bomse et al., Phys. Rev. 158, 1298 (1967)

       J. Fisk et al., International Conference on
       High Energy Physics, CERN, 358 (1962)

       E. Boldt er al., Phys. Rev. 133, B220 (1964)

11.   R.W. Bland, loc. cit.

       W. Chinowsky et al., loc. cit.

       F. Bomse et al., loc. cit.

12.   Sun Yin Fung et al., UCR-34 P107-72(unpublished)

13.   A.D. Brody et al., Phys. Lett. 34B, 655 (1971)

14.   L. Stodolsky and J.J. Sakurai, Phys. Rev.
       Lett. 11, 90 (1963)

15.   M. Ferro-Luzz er al., Nuovo Cimento 49A, 9(1967)

16.   D. Brown, UCRL 18254, 1968, (unpublished)

17.   W. De Baere et al., Nuovo Cimento 61A, 397
             (1969)

       G.S. Abrams et al., University of Illinois
       Report COO-1195-191 (1969)

18.   A. Bialas and K. Zalewski, Nuc. Phys. B6
       465 (1968)

19.   R.H. Dalitz, Phil Mag. 44, 1068 (1953)

20.   P. Eberhard and M. Pripstein, Phys. Rev.
       Lett. 10, 351 (1963)